Numerical simulations of rarefied gases in curved channels: thermal creep, circulating flow, and pumping effect

Kazuo Aoki[1], Pierre Degond [2] [3], Luc Mieussens[4]

Abstract. We present numerical simulations of a new system of micro-pump based on the thermal creep effect described by the kinetic theory of gases. This device is made of a simple smooth and curved channel with a periodic temperature distribution. Using the Boltzmann-BGK model as the governing equation for the gas flow, we develop a numerical method based on a deterministic finite volume scheme, implicit in time, with an implicit treatment of the boundary conditions. This method is comparatively less sensitive to the slow flow velocity than the usual Direct Simulation Monte Carlo method in case of long devices, and turns out to be accurate enough to compute macroscopic quantities like the pressure field in the channel. Our simulations show the ability of the device to produce a one-way flow that has a pumping effect.

Key words. Knudsen compressor, thermal creep flow, transpiration flow, BGK model, implicit scheme

AMS subject classifications. 76P05, 82B40, 82D05, 82C80, 65M06

1 Introduction

In the vicinity of solid boundaries, flows of rarefied gases show a large variety of phenomena that do not exist for dense gases as described by continuous gas dynamics (like Stokes or Navier-Stokes equations). For instance, several effects due to a temperature field applied on a solid boundary have been observed that cannot be explained in the framework of classical gas dynamics: let us mention thermal stress slip flow, nonlinear thermal stress

---

[1]Department of Mechanical Engineering and Science, Graduate School of Engineering, Kyoto University, Kyoto 606-8501, Japan (`aoki@aero.mbox.media.kyoto-u.ac.jp`)

[2]Université de Toulouse; UPS, INSA, UT1, UTM ;
Institut de Mathématiques de Toulouse ;
F-31062 Toulouse, France.

[3]CNRS; Institut de Mathématiques de Toulouse UMR 5219 ;
F-31062 Toulouse, France. (`degond@mip.ups-tlse.fr`)

[4]Université de Bordeaux, Institut de Mathématiques de Bordeaux, 351, cours de la Libération, 33405 Talence cedex, France (`Luc.Mieussens@math.u-bordeaux1.fr`) This research was supported partially by "Projet International de Coopération Scientifique (PICS)" of CNRS (grant n. 3195), by grants-in-aid for scientific research from JSPS (No. 17360041) and from MEXT (No. 1765033); computational resources have been provided by the CALMIP project (Calcul en Midi-Pyrénées), University Paul Sabatier, Toulouse, France. The work of L.M. was done when he was assistant professor at the Université de Toulouse, France.

flow, flow induced near a heated plate edge, thermophoresis, and thermal creep flow (see Sone [35, 36, 37]). This last phenomenon was already described (as thermal transpiration) by Reynolds in 1879 [32]: in a rarefied gas contained in a pipe whose temperature has a gradient along its axis, a flow is induced in the direction of the gradient, and this flow has a pumping effect, while the device does not involve any moving part or mixing process. This was also studied by Maxwell [25], and later by Knudsen [22, 23]. However, it is much more recently that a complete and accurate analysis on the basis of the Boltzmann equation has been proposed by Sone [34] (see also Ohwada, Sone and Aoki [30]). See also a continuum theory of this phenomenon proposed by Bielenberg and Brenner [8]. Recently, interest in this kind of flows is growing in connection with micro machine engineering, like Micro-Electro-Mechanical Systems (see Karniadakis, Beskok and Aluru [21] and Cercignani [13]). Indeed, the thermal creep is observed only if the gas is rarefied, that is to say when the characteristic length scale of the device containing the gas is not large with respect to its mean free path. This implies that one needs to use either very low pressure conditions, or a very small device (for instance, for the air at atmospheric pressure, the characteristic size of the device should be of the order of 0.1 microns). Different systems have recently been proposed to design pumping systems using this effect. They are often called Knudsen compressors (e.g., Pham-Van-Diep et al. [31]), since Knudsen himself in 1909 [22] described the first experimental device of this kind. The basic idea is to use cascade systems whose single unit is a pipe composed of a thin part connected to a thicker part.

In this paper, a simple device proposed in Aoki et al. [2, 3] is considered: the thermal creep flow is created by applying a periodic temperature field along a simple curved channel. As opposed to previous systems, we do not use any complex connection part. Up to our knowledge, such a device had not been investigated before. Since any experimental study of such micro-systems is a difficult challenge, our aim here is to use numerical simulations to demonstrate that our device can effectively produce a one-way flow. We also want to confirm that there exists a pumping effect in the corresponding cascade system [2, 3], which means that it is indeed a Knudsen compressor. However, large numerical simulations of rarefied gas problems are still a delicate issue, since this always implies using a large number of degrees of freedom. Indeed, even for two-dimensional plane flows, the distribution function of the particle velocities of the gas has six independent variables.

For that purpose, we propose a fast deterministic numerical method to accurately simulate rarefied gas flows. Actually, the most used numerical method for rarefied gases is the direct simulation Monte-Carlo method (DSMC) proposed by Bird [9]. It is a very robust and efficient method, now very well understood, in which complex physics can be included. However it remains that this method is intrinsically an unsteady method in which the numerical time scale must be smaller than the physical time scale to compute the flow with enough accuracy. This makes the DSMC method sometimes difficult to use when one is interested in computing slow flows for which the steady state is reached after very long transients. In such cases, the computational time needed to accurately capture the steady solution can be huge (see an example in section 5.4). Nevertheless, it has already been shown in [43, 5] that DSMC can be used in the context of Knudsen compressors (see also the numerical study of

a Knudsen compressor made by Alexeenko et al. [1] with computations based on both the DSMC method and the BGK model).

There also exist deterministic methods that use finite difference approximations of the Boltzmann equation. We mention for instance the works of Rogier and Schneider [33], Buet [11], or the works of Aristov and collaborators cited in [6]. Recently, for some simple interaction potentials, fast approximations of the Boltzmann collision operator have been proposed that considerably reduce its computational complexity (see Bobylev and Rjasanow [10], Filbet, Mouhot and Pareschi [15]). However, all these methods generally make use of the same splitting strategy between collision and transport process (as in the DSMC method). This technique suffers from severe time step restrictions that can be prohibitive for steady state calculations. Up to our knowledge, there are few methods for which the steady Boltzmann equation is directly solved. We mention the works of Ohwada [29] and Sone and Takata [42] in which a very accurate discretization accounts for possible discontinuities of the distribution function. However, these methods are restricted to very simple geometries, in particular due to their marching-in-space algorithm.

Here we propose a different approach in which we apply classical computational fluid dynamics tools to the kinetic framework. First we consider the simpler Bhatnagar-Gross-Krook (BGK) model of the Boltzmann equation. While this simplification is not physically well justified, it allows to easily reduce the computational complexities of collisions. Moreover, it is useful to obtain qualitative informations on a rarefied flow, and it is known to give accurate results in some situations [16]. Then we discretize the unsteady BGK equation in two dimensional (2D) plane geometries by a finite volume scheme using structured meshes on arbitrary curvilinear grids. The steady state is rapidly reached by using a linearized time implicit scheme. This implicit time discretization can be viewed as a compromise between a direct solving of the steady equation by a Newton-Raphson procedure and an unsteady computation. It allows to take very large time steps without stability problems. With the linearization procedure, the use of expensive algebraic nonlinear solvers is avoided. Moreover, as it is classical in numerics for kinetic equations, we use a robust velocity discretization of the collision operator that preserves the physical properties of conservation and entropy. Our approach is an extension of a method developed by one of the authors in [26, 27] for which we propose two major modifications: first, due to the simple structure of the 2D plane BGK equation, we are able to use the reduced distribution technique [19] to remove the dependency of the distribution function on the third component of the particle velocity. This reduces the number of dimensions of the problem from 5 to 4. Second, we propose a new implicit time discretization of the boundary conditions in order to speed up the convergence of our algorithm towards steady state. The difficulty of such treatment is that the discretized convection operator is much more complicated: the boundary conditions introduce non local terms both in space positions and velocities. Usually, these terms are set to 0 by using an explicit time discretization of the boundary conditions, but this is observed to give a poorly convergent algorithm, in particular in the present case of long cascade systems. Here, we introduce a simple implicit treatment that naturally makes use of the iterative linear solver used in the scheme. This modification considerably speeds up the algorithm for some partic-

ularly long computations. This numerical method has been implemented in a parallel code which turns out to be very robust and flexible enough to treat various gas kinetic simulation problems.

This method is then used to investigate the ability of our device to generate circulating flows and pumping effects. The accuracy of our computation reveals the complex structure of the flow in our device. We also investigate the pumping effect obtained with a various number of units in our cascade system. Although DSMC computations in such cases are expensive in terms of CPU time, we make several comparisons between this method and our deterministic results that demonstrate both the accuracy of our approach as well as its performance in terms of computational time.

The outline of this paper is the following. In section 2, we briefly give some elements of kinetic theory needed to present our method, and we give some details on the thermal creep flow mechanism. In section 3, a rapid review of previous Knudsen compressors is presented, and our device is detailed. The numerical method is presented in section 4, while some details are left to appendices A and B. Finally, we present our simulation results in section 5.

2 Rarefied gases and thermal creep flow

2.1 Kinetic description of a rarefied gas

In kinetic theory, a monoatomic gas is described by the distribution function $F(t, \mathbf{x}, \mathbf{v})$ defined such that $F(t, \mathbf{x}, \mathbf{v})d\mathbf{x}d\mathbf{v}$ is the mass of molecules that at time t are located in an elementary space volume $d\mathbf{x}$ centered in $\mathbf{x} = (x, y, z)$ and have a velocity in an elementary volume $d\mathbf{v}$ centered in $\mathbf{v} = (v_x, v_y, v_z)$.

Consequently, the macroscopic quantities as mass density ρ, momentum $\rho\mathbf{u}$ and total energy E are defined as the five first moments of F with respect to the velocity variable, namely:

$$(\rho(t, \mathbf{x}), \rho\mathbf{u}(t, \mathbf{x}), E(t, \mathbf{x})) = \int_{\mathbb{R}^3} (1, \mathbf{v}, \frac{1}{2}|\mathbf{v}|^2)F(t, \mathbf{x}, \mathbf{v}) \, d\mathbf{v}. \tag{1}$$

The temperature T of the gas is defined by the relation $E = \frac{1}{2}\rho|\mathbf{u}|^2 + \frac{3}{2}\rho RT$, where R is the gas constant defined as the ratio between the Boltzmann constant and the molecular mass of the gas.

When the gas is in a thermodynamical equilibrium state, it is well known that the distribution function F is a Gaussian function $\mathcal{M}[\rho, \mathbf{u}, T]$ of $\mathbf{v}$, called Maxwellian distribution, that depends only on the macroscopic quantities as

$$\mathcal{M}[\rho, \mathbf{u}, T] = \frac{\rho}{(2\pi RT)^{\frac{3}{2}}} \exp(-\frac{|\mathbf{v} - \mathbf{u}|^2}{2RT}). \tag{2}$$

It can easily be checked that $\mathcal{M}$ satisfies relations (1).

If the gas is not in a thermodynamical equilibrium state, its evolution is described by the following kinetic equation

$$\partial_t F + \mathbf{v} \cdot \nabla_{\mathbf{x}} F = Q(F), \tag{3}$$

which means that the total variation of F (described by the left-hand side) is due to the collisions between molecules (described by the right-hand side). The most realistic collision model is the Boltzmann operator but it is still very computationally expensive to use. In this paper, we prefer to use the simpler BGK model [7, 47]

$$Q(F) = \frac{1}{\tau}(\mathcal{M}[\rho, \mathbf{u}, T] - F) \tag{4}$$

which models the effect of the collisions as a relaxation of F towards the local equilibrium corresponding to the macroscopic quantities defined by (1). The relaxation time is defined as $\tau = \frac{\mu}{\rho RT}$, where μ is the viscosity of the gas. This definition allows to match the correct viscosity in the Navier-Stokes equations obtained by the Chapman-Enskog expansion. This viscosity μ is usually supposed to fit the following law $\mu = \mu_{ref}(\frac{T}{T_{ref}})^\omega$, where μ_{ref} and T_{ref} are reference viscosity and temperature determined experimentally for each gas, as well as the exponent ω (see a table in [9]). In this paper, we shall use the simplest law obtained with $\omega = 1$. This corresponds to the viscosity law obtained with the Boltzmann equation for Maxwellian molecules [12].

2.2   Interaction with the boundaries

Modeling gas-surface interactions is an important problem, still the subject of current research. In this work, we shall use the classical and simple diffuse reflection model. The influence of other interaction models on the results presented in this paper is deferred to a future work.

Let us suppose that the boundary has a velocity $\mathbf{u}_w$ and temperature T_w. In the diffuse reflection model, a molecule that collides with this boundary is supposed to be re-emitted with a temperature equal to T_w, and with a random velocity normally distributed around $\mathbf{u}_w$. This reads

$$F(t, \mathbf{x}, \mathbf{v}) = \sigma \mathcal{M}[1, \mathbf{u}_w, T_w](\mathbf{v}) \tag{5}$$

if $\mathbf{v} \cdot \mathbf{n}(\mathbf{x}) > 0$, where $\mathbf{n}(\mathbf{x})$ is the normal to the wall at point $\mathbf{x}$ directed into the gas. The parameter σ is defined such that there is no normal mass flux across the boundary (all the molecules are re-emitted). Namely, that is,

$$\sigma = -\left(\int_{\mathbf{v}\cdot\mathbf{n}(\mathbf{x})<0} F(t, \mathbf{x}, \mathbf{v})\mathbf{v} \cdot \mathbf{n}(\mathbf{x})\,d\mathbf{v}\right) \Big/ \left(\int_{\mathbf{v}\cdot\mathbf{n}(\mathbf{x})>0} \mathcal{M}[1, \mathbf{u}_w, T_w](\mathbf{v})\mathbf{v} \cdot \mathbf{n}(\mathbf{x})\,d\mathbf{v}\right). \tag{6}$$

2.3   Thermal creep flow

Without describing the theory in detail, we only give below a simple explanation (taken from [36]) of the thermal creep physical mechanism. Consider a point A of the boundary

5

(see figure 1) and the molecules that impact this point. Since the boundary is hotter at the right of A than at the left, then the molecules coming from the right have a greater average kinetic energy than those coming from the left. Consequently these molecules transfer a momentum to A which is greater than the momentum transferred by left molecules. On the other hand, the molecules reflected diffusely on the boundary do not contribute to the tangential momentum transfer. Therefore the gas transfers a momentum to the boundary in the opposite direction to the temperature gradient (that is to say, from the right to the left). Finally, since the boundary is at rest, by reaction it transfers a force to the gas directed from the left to the right. This produces a flow directed in the direction of the temperature gradient. This flow is called thermal creep flow. Note that this phenomenon disappears in the continuous (dense) regime.

This effect suggests that it is possible to create a gas flow without any mechanical part. This has been studied for a long time (see the numerous references given in [36], section 3.11.6). Several experimental studies have clearly demonstrated the practical possibility to use this phenomenon to create a pumping system, which is described in section 3.1.

3 Pumping systems using the thermal creep

3.1 Pumping effect and Knudsen compressors

The basic idea of the Knudsen compressors is the following: when two reservoirs are joined by a pipe with a temperature gradient, classical fluid mechanics predicts that at steady state the pressure is constant in the device. But if the pipe is thin enough, so that the gas contained in the pipe is slightly rarefied, then a thermal creep flow is generated by the temperature gradient in the direction of this gradient. A small amount of gas is then pumped out of the reservoir of lower temperature and sent into the reservoir of higher temperature. This creates a small pressure difference between the two reservoirs, which is called the pumping effect.

However, this pressure difference is very small. It can be increased by using a larger temperature gradient, but of course, this gradient cannot be increased indefinitely. Knudsen suggested to use a cascade system in which a basic unit is composed of a pipe with a temperature gradient connected to a section with an opposed temperature gradient so that the two ends of the unit are kept at the same temperature. Of course, these two gradients create two opposed thermal creep flows. The pipe and the connecting section must be designed so that these flows do not cancel each other, and it is hoped that a global mass flow will be generated.

With the growing of MEMS technology, several modern versions of the Knudsen compressor have been proposed. For instance Pham-Van-Diep et al. [31] and Vargo and Muntz [46] studied the pressure difference obtained with a Knudsen compressor in which capillary pipes are obtained by using a thin membrane (see also Hudson and Bartel [20], Han et al. [17], and also [1]). Another strategy (without membrane) was proposed by Sone, Waniguchi and Aoki [43] and Aoki et al [5] who used a cascade system of channels or pipes with a periodic

temperature. A basic unit is composed of a pipe with an increasing temperature in the first part, and a decreasing temperature in the second part. The opposite thermal creep of the second part is maintained in a recirculation flow in a ditch dug along the pipe. Then a global mass flow due to the thermal creep of the first part is generated in the unit. A pumping effect is also observed in the case of a system closed at both ends. This has been investigated both numerically and experimentally in [43, 5, 39, 41].

Using this last idea, we present in the following section a device that could be used as a Knudsen compressor.

3.2   A device using curved channels

While the previous systems have been proved to be very efficient, their geometrical structure is not very simple. In particular, it seems difficult to use them for small systems as MEMS. Here, we propose to use a simple smooth channel with curved boundaries ([2, 3]). This should be much simpler to realize on MEMS.

Basically a single unit of our device is detailed in figure 2. It has a hook shape that is composed of a straight channel joined to a circular curved part. A uniform temperature gradient is applied to the straight part (the temperature increases linearly from T_L to T_H along the channel), while an opposed temperature gradient is applied to the curved part. For the same reasons as explained in section 3.1, it is expected that two opposed thermal creep flows will be generated in the different parts. Due to the different geometries of these parts, one can hope that one of these flows should be stronger than the other one. Then a global net flow should be created.

Consequently, the first test we propose is to generate a circulating flow by joining one unit and its symmetric image to form a ring as described in figure 3.

A similar test consists in joining one unit to its symmetric mirror image to form an S shape (see figure 4). Then periodic boundary conditions can be applied to both ends to generate an infinite cascade of S shapes.

Note that these two tests can be simulated by using only one unit as in figure 2 and appropriate "periodic" boundary conditions at both ends (see below).

The second test we propose is similar to the previous cascade system, except that we use a finite number N of units as described in figure 5. Moreover, this system is closed at both ends to create a pumping effect. Namely, we want to observe that pressure and density differences can be maintained at steady state between the two ends.

It should be mentioned that we have investigated the same problem using the DSMC method and observed that the idea mentioned above actually works [2].

The boundary conditions we use are diffuse reflection on the straight and curved boundaries (as detailed in section 2.2). For the circulating flow in the ring shape, we apply the following symmetry periodic boundary conditions at both ends A and B of a single unit

$$F(t, A, v_x, v_y, v_z) = F(t, B, -v_x, -v_y, v_z). \tag{7}$$

For the one-way flow in the infinite cascade of S shapes, we apply this different symmetry

7

periodic boundary condition

$$F(t, A, v_x, v_y, v_z) = F(t, B, -v_x, v_y, v_z). \tag{8}$$

Note that even if the flow is subsonic, the kinetic setting which is used here does not require any subsonic boundary conditions, as opposed to Navier-Stokes equations, for instance. Finally, for the pumping system, the diffuse reflection condition is applied to both ends with the low temperature T_L.

In the next sections, we detail our numerical method to solve the BGK equation in these three different devices. However, note that for computational cost reasons, this study is restricted to plane channels. That is to say, figures 3, 4, and 5 represent constant sections of channels that are infinite in the direction orthogonal to the figures. More realistic circular pipes would require full 3D computations, which is at present far from being reachable, in particular with the third device in case of a large number of units.

4 Numerical method

4.1 Reduced BGK model

In case of plane flows, F is independent of z and hence the transport operator in (3) does not contain explicitly the velocity v_z.

Consequently, the computational complexity of the BGK equation (3) can be reduced by using the classical reduced distribution technique (first introduced—up to our knowledge— by Huang and Hwang for polyatomic gases in [19]). This approach is widely used to compute 2D flows, see for instance [48, 4, 38]. For the sake of completeness, this method is briefly described below.

We define the reduced distribution functions

$$f(t, x, y, v_x, v_y) = \int_{\mathbb{R}} F \, dv_z,$$

$$g(t, x, y, v_x, v_y) = \int_{\mathbb{R}} \frac{1}{2} v_z^2 F \, dv_z.$$

Now we denote by $v = (v_x, v_y)$ and $x = (x, y)$ the 2-dimensional velocity and position variables. By symmetry the macroscopic velocity $\mathbf{u}$ has no component along z and we shall denote accordingly by $u = (u_x, u_y)$ its component in the plane (x, y). Then it is easy to show that f and g are solutions of the following coupled system of relaxation equations

$$\partial_t f + v \cdot \nabla_x f = \frac{1}{\tau}(M[\rho, u, T] - f),$$

$$\partial_t g + v \cdot \nabla_x g = \frac{1}{\tau}(\frac{RT}{2}M[\rho, u, T] - g),$$

$$\tag{9}$$

where $M[\rho, u, T]$ is the reduced Maxwellian defined by

$$M[\rho, u, T] = \int_{\mathbb{R}} \mathcal{M}[\rho, \mathbf{u}, T] \, dv_z = \frac{\rho}{2\pi RT} \exp(-\frac{|v - u|^2}{2RT}),$$

8

and the macroscopic quantities are obtained through f and g by

$$\rho = \int_{\mathbb{R}^2} f \, d\mathrm{v},$$

$$\rho\mathrm{u} = \int_{\mathbb{R}^2} \mathrm{v} f \, d\mathrm{v}, \tag{10}$$

$$T = \frac{1}{\frac{3}{2}\rho R} \int_{\mathbb{R}^2} (\frac{1}{2}|\mathrm{v} - \mathrm{u}|^2 f + g) \, d\mathrm{v}.$$

With this procedure, the variable v_z is eliminated. Consequently, system (9) is computationally less expensive than (3).

Note that the second distribution function g is necessary to obtain a closed system of equations. Indeed, the temperature T is defined through the integral of $(v_x^2 + v_y^2 + v_z^2)F$, and hence it cannot be defined through the reduced distribution f only. Consequently, the first equation of (9) is not closed if g is not used. Also note that the reduced distributions f and g as well as the macroscopic quantities are indeed those of the full distribution F without any approximation. Once the macroscopic quantities are obtained, F can be reconstructed easily from the original equation (3) with (4) that is just a differential equation for F.

4.2   Velocity discretization

Here we propose a robust velocity discretization of (9). This approach is based on the work of Mieussens in [26, 27] (see also a similar extension for a reduced BGK model for polyatomic gases in [14]). The main idea is to design a discretization of the Maxwellian distribution $M[\rho, \mathrm{u}, T]$ such that the discretized version of (9) satisfies the same properties as the continuous one, namely conservation and entropy properties. We refer to [28, 14] for mathematical proofs of existence and consistency results for such approximations.

More precisely, we define a Cartesian grid $\mathcal{V}$ of N_v nodes $\mathrm{v_k} = (v_x^k = a + k\Delta v_x, v_y^l = b + l\Delta v_y)$ where $\mathrm{k} = (k, l)$ is a couple of bounded indexes. We denote by f_k and g_k the approximations of $f(\mathrm{v_k})$ and $g(\mathrm{v_k})$. The macroscopic quantities are now defined by using a simple rectangle quadrature as

$$\rho = \sum_\mathrm{k} f_\mathrm{k} \Delta \mathrm{v},$$

$$\rho\mathrm{u} = \sum_\mathrm{k} \mathrm{v_k} f_\mathrm{k} \Delta \mathrm{v}, \tag{11}$$

$$E = \frac{1}{2}|\mathrm{u}|^2 + \frac{3}{2}\rho RT = \sum_\mathrm{k} (\frac{1}{2}|\mathrm{v_k}|^2 f_\mathrm{k} + g_\mathrm{k})\Delta \mathrm{v},$$

where $\Delta \mathrm{v} = \Delta v_x \Delta v_y$. For clarity, we now introduce the following 4-dimensional vectors

$$\vec{\rho} = (\rho, \rho\mathrm{u}, E)^T, \qquad \vec{m}(v) = (1, \mathrm{v}, \frac{1}{2}|\mathrm{v}|^2)^T, \qquad \vec{e} = (0, 0, 0, 1)^T.$$

9

Then the previous relations (11) read in a very compact form

$$\vec{\rho} = \sum_{k} (\vec{m}(v_k) f_k + \vec{e}\, g_k)\, \Delta v. \tag{12}$$

These notations allow to simplify the writing of the velocity discretization of (9). This approximation now is

$$\partial_t f_k + v_k \cdot \nabla_x f_k = \frac{1}{\tau}(M_k[\vec{\rho}] - f_k),$$
$$\partial_t g_k + v_k \cdot \nabla_x g_k = \frac{1}{\tau}(N_k[\vec{\rho}] - g_k), \tag{13}$$

where $M_k[\vec{\rho}]$ and $N_k[\vec{\rho}]$ are approximations of $M[\rho, u, T](v_k)$ and $\frac{RT}{2} M[\rho, u, T](v_k)$ defined to ensure that the discrete BGK system (13) satisfies the same properties of conservation and entropy as the continuous model (9). Namely we have

$$M_k[\vec{\rho}] = \exp(\vec{\alpha}(\vec{\rho})^T \vec{m}(v_k)), \qquad N_k[\vec{\rho}] = -\frac{1}{2\alpha_4(\vec{\rho})} M_k[\vec{\rho}], \tag{14}$$

where $\vec{\alpha} = (\alpha_1, \alpha_2, \alpha_3, \alpha_4)^T$ is the solution of the following non linear 4×4 system

$$\sum_{k} \vec{m}(v_k) \exp(\vec{\alpha}(\vec{\rho})^T \vec{m}(v_k)) \Delta v - \frac{\rho}{2\alpha_4(\vec{\rho})} \vec{e} = \vec{\rho}. \tag{15}$$

Note that in the continuous case (that is to say with integrals on $\mathbb{R}^2$ instead of quadratures), we have an explicit relation between $\vec{\alpha}(\vec{\rho})$ and $\vec{\rho}$, namely

$$\vec{\alpha}(\vec{\rho}) = \left(\log\left(\frac{\rho}{2\pi RT} \right) - \frac{|u|^2}{2RT}, \frac{u}{RT}, -\frac{1}{RT} \right)^T. \tag{16}$$

This relation is not valid in the discrete case, but it is used in our code to solve nonlinear system (15) by a Newton algorithm.

4.3 Linearized implicit scheme

Here we propose a time and space discretization of the system of the reduced discrete BGK equations (13).

Consider a spatial Cartesian grid defined by nodes $(x_i, y_j) = (i\Delta x, j\Delta y)$ and cells $]x_{i-\frac{1}{2}}, x_{i+\frac{1}{2}}[\times]y_{j-\frac{1}{2}}, y_{j+\frac{1}{2}}[$ for $i = 1$ to i_{max} and $j = 1$ to j_{max}. The number of cells is denoted by $N_c = i_{max} j_{max}$. Consider also a time discretization with $t_n = n\Delta t$. If $f_{k,i,j}^n$ and $g_{k,i,j}^n$ are approximations of $f_k(t_n, x_i, y_j)$ and $g_k(t_n, x_i, y_j)$, the moments $\vec{\rho}$ defined by (12) are naturally approximated by

$$\vec{\rho}_{i,j}^n = \sum_{k} (\vec{m}(v_k) f_{k,i,j}^n + \vec{e}\, g_{k,i,j}^n)\, \Delta v.$$

The transport part of (13) is approximated by a standard finite volume scheme which has second order accuracy in space. For the nonlinear relaxation term, a standard centered approximation technique is used. Our scheme thus reads

$$f_{k,i,j}^{n+1} = f_{k,i,j}^n \quad - \quad \frac{\Delta t}{\Delta x}\left(\mathcal{F}_{i+\frac{1}{2},j}(f_k^n) - \mathcal{F}_{i-\frac{1}{2},j}(f_k^n)\right) - \frac{\Delta t}{\Delta y}\left(\mathcal{F}_{i,j+\frac{1}{2}}(f_k^n) - \mathcal{F}_{i,j-\frac{1}{2}}(f_k^n)\right)$$

$$+ \quad \frac{\Delta t}{\tau_{i,j}^n}(M_k[\vec{\rho}_{i,j}^n] - f_{k,i,j}^n), \tag{17}$$

$$g_{k,i,j}^{n+1} = g_{k,i,j}^n \quad - \quad \frac{\Delta t}{\Delta x}\left(\mathcal{F}_{i+\frac{1}{2},j}(g_k^n) - \mathcal{F}_{i-\frac{1}{2},j}(g_k^n)\right) - \frac{\Delta t}{\Delta y}\left(\mathcal{F}_{i,j+\frac{1}{2}}(g_k^n) - \mathcal{F}_{i,j-\frac{1}{2}}(g_k^n)\right)$$

$$+ \quad \frac{\Delta t}{\tau_{i,j}^n}(N_k[\vec{\rho}_{i,j}^n] - g_{k,i,j}^n)$$

where the numerical fluxes are defined for every grid function $\{\varphi_{k,i,j}\}$ by

$$\mathcal{F}_{i+\frac{1}{2},j}(\varphi_k) \quad = \quad \frac{1}{2}\left(v_x^k(\varphi_{k,i+1,j} + \varphi_{k,i,j}) - |v_x^k|(\Delta\varphi_{k,i+\frac{1}{2},j} - \Phi_{k,i+\frac{1}{2},j}^n)\right)$$

$$\mathcal{F}_{i,j+\frac{1}{2}}(\varphi_k) \quad = \quad \frac{1}{2}\left(v_y^l(\varphi_{k,i,j+1} + \varphi_{k,i,j}) - |v_y^l|(\Delta\varphi_{k,i,j+\frac{1}{2}} - \Phi_{k,i,j+\frac{1}{2}}^n)\right) \tag{18}$$

with the notation $\Delta\varphi_{k,i+\frac{1}{2},j} = \varphi_{k,i+1,j} - \varphi_{k,i,j}$, and the flux limiter function $\Phi_{k,i+\frac{1}{2},j}^n$ allows to obtain a second order scheme. Note that according to section 4.2, the discrete equilibria $M_k[\vec{\rho}_{i,j}^n]$ and $N_k[\vec{\rho}_{i,j}^n]$ are defined for each cell (i,j) through relations (14) and (15) by using $\vec{\rho}_{i,j}^n$ instead of $\vec{\rho}$ in the formula.

When indexes i and j correspond to cells located at the boundaries of the domain, there appear unknown values in the numerical fluxes, like $f_{k,0,j}^n$, $f_{k,i_{max}+1,j}^n$, $f_{k,i,0}^n$, $f_{k,i,j_{max}+1}^n$ for the first order scheme. Corresponding cells $(0,j)$, $(i_{max}+1,j)$, $(i,0)$, $(i,j_{max}+1)$ are called ghost-cells. These values are classically defined according to the boundary conditions (B.C for short) specified for the problem. Here we consider two types of B.C: diffuse reflections, that are local in space but global in velocities, and symmetry periodic conditions, that couple two different cells and two symmetric velocities. For instance, incident molecules in a boundary cell of indexes $(i, j = 1)$ are supposed to be re-emitted by the wall from a ghost cell of indexes $(i, 0)$. This cell is the mirror cell of $(i, 1)$ with respect to the wall. The diffuse reflection (5) is then modeled by

$$(f_{k,i,0}^n, g_{k,i,0}^n) = \sigma_{i,1}\left(M_k[1, u_w, T_w], N_k[1, u_w, T_w]\right), \quad v_k \cdot n_{i,1} > 0, \tag{19}$$

where $\sigma_{i,1}$ is determined so as to avoid a mass flux across the wall, *i.e.* between cells $(i, 0)$ and $(i, 1)$. Relation (6) gives

$$\sigma_{i,1} = -\frac{\sum_{v_k \cdot n_{i,1} < 0} v_k \cdot n_{i,1}\, f_{k,i,1}^n \Delta v}{\sum_{v_k \cdot n_{i,1} > 0} v_k \cdot n_{i,1}\, M_k[1, u_w, T_w]\Delta v}.$$

For the symmetry periodic B.C of the ring shaped channel, relation (7) gives

$$f_{k,0,j}^n = f_{k',i_{max},j}^n, \tag{20}$$

11

where k' is such that $v_{k'} = -v_k$. Finally, the symmetry periodic B.C (8) for the infinite cascade of S shaped channel gives the same relation with now k' such that $v_{k'} = (-v_x^k, v_y^l)$.

This scheme can also be written for curvilinear meshes as we did for the numerical simulations of section 5. But to simplify the presentation, this is not presented here (see an example for a single distribution BGK model in [27]).

Since this scheme is explicit, the CFL condition can be very restrictive, in particular for steady state computations. A classical way to overcome this difficulty is to use an implicit scheme. It is derived from the explicit scheme by evaluating at t_{n+1} the transport and relaxation terms responsible for stability problems with large Δt. This scheme reads

$$
f_{k,i,j}^{n+1} = f_{k,i,j}^n \quad - \quad \frac{\Delta t}{\Delta x}\left(\mathcal{F}_{i+\frac{1}{2},j}(f_k^{n+1}) - \mathcal{F}_{i-\frac{1}{2},j}(f_k^{n+1})\right) - \frac{\Delta t}{\Delta y}\left(\mathcal{F}_{i,j+\frac{1}{2}}(f_k^{n+1}) - \mathcal{F}_{i,j-\frac{1}{2}}(f_k^{n+1})\right)
$$
$$
+ \quad \frac{\Delta t}{\tau_{i,j}^n}(M_k[\vec{\rho}_{i,j}^{n+1}] - f_{k,i,j}^{n+1}), \tag{21}
$$
$$
g_{k,i,j}^{n+1} = g_{k,i,j}^n \quad - \quad \frac{\Delta t}{\Delta x}\left(\mathcal{F}_{i+\frac{1}{2},j}(g_k^{n+1}) - \mathcal{F}_{i-\frac{1}{2},j}(g_k^{n+1})\right) - \frac{\Delta t}{\Delta y}\left(\mathcal{F}_{i,j+\frac{1}{2}}(g_k^{n+1}) - \mathcal{F}_{i,j-\frac{1}{2}}(g_k^{n+1})\right)
$$
$$
+ \quad \frac{\Delta t}{\tau_{i,j}^n}(N_k[\vec{\rho}_{i,j}^{n+1}] - g_{k,i,j}^{n+1})
$$

The relaxation time is kept explicit, and for the second order scheme, the flux limiters (non differentiable) are kept explicit too. However this scheme is still nonlinear due to the equilibria $M_k[\vec{\rho}_{i,j}^{n+1}]$ and $N_k[\vec{\rho}_{i,j}^{n+1}]$. As usual in hyperbolic implicit schemes, these terms are linearized as follows

$$
M_k[\vec{\rho}_{i,j}^{n+1}] \approx M_k[\vec{\rho}_{i,j}^n] + \partial_{\vec{\rho}}M_k[\vec{\rho}_{i,j}^{n+1}](\vec{\rho}_{i,j}^{n+1} - \vec{\rho}_{i,j}^n),
$$
$$
N_k[\vec{\rho}_{i,j}^{n+1}] \approx N_k[\vec{\rho}_{i,j}^n] + \partial_{\vec{\rho}}N_k[\vec{\rho}_{i,j}^{n+1}](\vec{\rho}_{i,j}^{n+1} - \vec{\rho}_{i,j}^n),
$$

where $\partial_{\vec{\rho}}M_k[\vec{\rho}_{i,j}^{n+1}]$ and $\partial_{\vec{\rho}}N_k[\vec{\rho}_{i,j}^{n+1}]$ are the Jacobian matrices of the mappings $\vec{\rho} \mapsto M_k[\vec{\rho}]$ and $\vec{\rho} \mapsto N_k[\vec{\rho}]$. See appendix A for detailed expressions of these Jacobian matrices.

For implementation, it is useful to store all the unknowns into a single large 2-block vector $U^n = (f^n, g^n)$, with blocks $f^n = \{f_k^n\}_k$ and $g^n = \{g_k^n\}_k$. The sub-blocks f_k^n and g_k^n are then stored as $f_k^n = \{f_{k,i,j}^n\}_{k,i,j}$ and $g_k^n = \{g_{k,i,j}^n\}_{k,i,j}$. Then the linearized implicit scheme is rewritten under this δ matrix-form

$$
\left(\frac{I}{\Delta t} + T + R^n\right)\delta U^n = RHS^n, \tag{22}
$$

where $\delta U^n = U^{n+1} - U^n$, I is the unit matrix, T is a matrix such that for every 2-block vector $V = (\varphi, \psi)$

$$
TV = \left(\left\{\frac{1}{\Delta x}\left(\mathcal{F}_{i+\frac{1}{2},j}(\varphi_k) - \mathcal{F}_{i-\frac{1}{2},j}(\varphi_k)\right) - \frac{1}{\Delta y}\left(\mathcal{F}_{i,j+\frac{1}{2}}(\varphi_k) - \mathcal{F}_{i,j-\frac{1}{2}}(\varphi_k)\right)\right\}_{k,i,j}\right.
$$
$$
\left., \left\{\frac{1}{\Delta x}\left(\mathcal{F}_{i+\frac{1}{2},j}(\psi_k) - \mathcal{F}_{i-\frac{1}{2},j}(\psi_k)\right) - \frac{1}{\Delta y}\left(\mathcal{F}_{i,j+\frac{1}{2}}(\psi_k) - \mathcal{F}_{i,j-\frac{1}{2}}(\psi_k)\right)\right\}_{k,i,j}\right) \tag{23}
$$

12

with only the first order fluxes. Moreover, the coefficient of T that would correspond to the boundary conditions are classically set to 0. This corresponds to set $\delta U^n = 0$, that is to say $f^{n+1} = f^n$ and $g^{n+1} = g^n$ at these cells. This is called an explicit treatment of the boundary conditions, since on the contrary the right-hand side defined in (25) contains indeed the boundary terms. This considerably simplifies the structure of T, since it is now a discrete convection operator with homogeneous Dirichlet B.C (see below).

The relaxation matrix R^n is such that for every 2-block vector $V = (\varphi, \psi)$

$$R^n V = \left(\left\{ \frac{1}{\tau_{i,j}^n} (\varphi_{\mathrm{k},i,j} - \partial_{\vec{\rho}} M_{\mathrm{k}}[\vec{\rho}_{i,j}^{n+1}] \vec{\rho}(V_{i,j})) \right\}_{\mathrm{k},i,j}, \left\{ \frac{1}{\tau_{i,j}^n} (\psi_{\mathrm{k},i,j} - \partial_{\vec{\rho}} N_{\mathrm{k}}[\vec{\rho}_{i,j}^{n+1}] \vec{\rho}(V_{i,j})) \right\}_{\mathrm{k},i,j} \right),$$
(24)

where we set $\vec{\rho}(V_{i,j}) = \sum_{\mathrm{k}} (\vec{m}(\mathrm{v_k}) \varphi_{\mathrm{k},i,j} + \vec{e} \psi_{\mathrm{k},i,j}) \Delta \mathrm{v}$. Finally, we set the right-hand side to

$$
\begin{aligned}
RHS^n &= \left(\left\{ -\frac{1}{\Delta x} \left(\mathcal{F}_{i+\frac{1}{2},j}(f_{\mathrm{k}}^n) - \mathcal{F}_{i-\frac{1}{2},j}(f_{\mathrm{k}}^n) \right) - \frac{1}{\Delta y} \left(\mathcal{F}_{i,j+\frac{1}{2}}(f_{\mathrm{k}}^n) - \mathcal{F}_{i,j-\frac{1}{2}}(f_{\mathrm{k}}^n) \right) \right. \right. \\
&\qquad \left. + \frac{1}{\tau_{i,j}^n} (M_{\mathrm{k}}[\vec{\rho}_{i,j}^n] - f_{\mathrm{k},i,j}^n) \right\}_{\mathrm{k},i,j} \\
&\qquad, \left\{ -\frac{1}{\Delta x} \left(\mathcal{F}_{i+\frac{1}{2},j}(g_{\mathrm{k}}^n) - \mathcal{F}_{i-\frac{1}{2},j}(g_{\mathrm{k}}^n) \right) - \frac{1}{\Delta y} \left(\mathcal{F}_{i,j+\frac{1}{2}}(g_{\mathrm{k}}^n) - \mathcal{F}_{i,j-\frac{1}{2}}(g_{\mathrm{k}}^n) \right) \right. \\
&\qquad \left. \left. + \frac{1}{\tau_{i,j}^n} (N_{\mathrm{k}}[\vec{\rho}_{i,j}^n] - f_{\mathrm{k},i,j}^n) \right\}_{\mathrm{k},i,j} \right),
\end{aligned}
$$
(25)

which contains the limiters for the second-order scheme and the boundary conditions.

Note that when our scheme (22) converges to steady state, the discrete steady solution necessarily satisfies $RHS^n = 0$. This discrete relation is independent of the time step (see the definition of the fluxes of (25) given in (18)). Consequently, our discrete solution is also independent of this time step.

It can be noted that relation (23) and (18) imply that T is a 2×2 block diagonal matrix, in which each block of the diagonal is itself a $N_v \times N_v$ block diagonal matrix. The sub-blocks—denoted by T_{k}—are $N_c \times N_c$ pentadiagonal matrices (see figure 6). Since the relaxation operator couples the velocities, but not the different space cells, the matrix R^n is a 2×2 block matrix, in which the blocks are $N_v \times N_v$ full block matrices. These sub-blocks are composed of $N_c \times N_c$ diagonal matrices denoted by $R_{\mathrm{k},\mathrm{k}'}^n$ on figure 6.

The linear system (22) to be solved at each iteration is very large, since its size is $2N_v N_c \times 2N_v N_c$. An iterative method well adapted to the different sparse structures of the matrices may then be used. First, we extend the algorithm proposed in [27], which is based on a coupling between Jacobi and Gauss-Seidel methods. At the level of its small $N_c \times N_c$ sub-blocks, R^n is separated into its block diagonal Δ^n and its block off-diagonal E^n, *i.e.* $R^n = \Delta^n - E^n$ (this is the Jacobi step). Then system (22) is equivalent to

$$\left(\frac{I}{\Delta t} + T + \Delta^n \right) \delta U^n = RHS^n + E^n \delta U^n.$$

Since the matrix of this linear system is block diagonal with pentadiagonal blocks $\frac{I}{\Delta t} + T_k + \Delta_k^n$ (see figure 6), it is possible to use a line Gauss-Seidel method by setting $T_k = M_k - N_k$. This gives the following algorithm:

Algorithm 4.1. set $V^{(0)} = 0$,
for $p = 0, \ldots, P$, **solve**

$$\left(\frac{I}{\Delta t} + M_k + \Delta_k^n \right) V_k^{(p+1)} = RHS_k^n + N_k V_k^{(p)} + [E^n V^{(p)}]_k, \quad \forall k \tag{26}$$

set $\delta U^n = V^{(P+1)}$.

The linear systems (26) may easily and exactly be solved by successive LU decompositions of tridiagonal matrices of $\mathbb{R}^{imax \times imax}$ or $\mathbb{R}^{jmax \times jmax}$. Note that we do not need to store nor to form the different matrices. Indeed, we only have to compute the coefficients of the diagonal blocks Δ_k^n of R^n (see appendix B for a detailed expression). The matrix-vector products of the right-hand side of (26) are just the results of formula similar to (23) and (24).

While the number of iterations of the linear solver may be very large to reach convergence to the exact solution, we only use a small number $P \leq 8$. This is sufficient for the global algorithm to reach steady state.

In fact, we explain in the following section how we propose to modify this linear solver to improve the speed of convergence by taking into account the boundary conditions more accurately.

4.4 Implicit boundary conditions

It is observed in some cases that the convergence of our algorithm is quite slow, in particular for long channels. Therefore it is natural to try to improve the treatment of the B.C so as to speed up this convergence.

In this section, we propose a simple implicit treatment of the B.C. The problem of fully implicit B.C is that it deteriorates the simple block structure of the transport matrix T. Indeed, the diffuse reflection introduces a coupling between different velocities and the symmetry periodic conditions introduce a coupling between very distant cells, as this can be seen in (19) and (20).

Consequently, for implicit boundary conditions, T is replaced in scheme (22) by the matrix $T + B$ where T is untouched and B contains all the boundary terms. We find

$$\left(\frac{I}{\Delta t} + T + B + R^n \right) \delta U^n = RHS^n, \tag{27}$$

Now, our algorithm 4.1 is modified as follows. Since system (27) is equivalent to $(\frac{I}{\Delta t} + T + \Delta^n) \delta U^n = RHS^n + E^n \delta U^n - B \delta U^n$, the matrix B can be treated in the right-hand side of (26), like the block off-diagonal E^n. Therefore, we can use the same line Gauss-Seidel method as in algorithm 4.1 to obtain:

Algorithm 4.2. set $V^{(0)} = 0$,
    for $p = 0, \ldots, P$, **solve**

$$\left(\frac{I}{\Delta t} + M_k + \Delta_k^n \right) V_k^{(p+1)} = RHS_k^n + N_k V_k^{(p)} + [E^n V^{(p)}]_k - [B V^{(p)}]_k, \quad \forall k \qquad (28)$$

    set $\delta U^n = V^{(P+1)}$.

Note that B is very sparse, even much sparser than T and R^n: it has at most $4(i_{max} + j_{max})N_v$ non-zero coefficients. Therefore, the additional cost of each iteration of this algorithm is very small, while we have observed that this simple modification speeds up the convergence of the global method to steady state.

4.5 Numerical comparisons with other methods

Our algorithm has been compared with the results obtained in [26, 27]. In these references, the BGK model (3)–(4) is solved with a similar algorithm, but with a single distribution function (with 3D velocity variables), and with an explicit treatment of the B.C. For 1D cases (as Couette flows and shock structure problem) and 2D cases (flow around a cylinder, compression ramp) we compared the pointwise values of the macroscopic quantities (density, velocity, temperature, pressure). We found that the two methods give almost indistinguishable results, while the present method is very much faster. Consequently, this shows that our algorithm accurately solves the BGK equation. Moreover, all the conclusions deduced in [26, 27] from various comparisons (such as DSMC, for instance) also apply to our method.

5 Numerical simulations

5.1 Parameters of the simulations

The circulating flow problem is characterized by four parameters. The two geometric ones are $\kappa = \frac{D}{R}$ that measures the ratio between the width of the channel to the radius of the circular part and $B = \frac{L_S}{L_S + \pi R}$ which is the ratio between the length of the straight pipe to the total length of one unit (see figure 2). The two physical parameters are the temperature ratio $\frac{T_H}{T_L}$ and the Knudsen number

$$Kn = \frac{l_0}{D} = \frac{\sqrt{2RT_L}}{D\rho_0 RT_{ref}/\mu_{ref}} \qquad (29)$$

where l_0 is the mean free path of the molecules at the equilibrium state at rest (ρ_0 is the global average density in the channel).

The pumping problem is characterized by these parameters and the number N of elementary units.

In the simulations presented here, only the parameters κ, Kn and N will vary. The temperature ratio $\frac{T_H}{T_L}$ is set to 3 and the length ratio B is set to 0.5.

The gas we use is argon of molecular mass $0.663\,10^{-20}$ kg, the initial velocity of the gas is zero, the low temperature T_L is set to 300 K, and consequently the high temperature T_H is set to 900 K.

The second order linearized implicit scheme is used in all the computations, with a CFL number of 1000 (*i.e.* Δt is 1000 times the explicit time step). The criterion used to determine whether the flow has reached steady state is the reduction of the quadratic global residual $\frac{1}{\Delta t}(\sum_{k,i,j}|RHS_{k,i,j}^n|^2)^{\frac{1}{2}}$ by a factor of 10^5.

The space domain is discretized by a curvilinear mesh with a uniform distribution of nodes on the boundaries. The number of mesh cells depend on the test case.

Note that the velocity grid is appropriately chosen for each case. Since the same grid is used in each point of space, it should be large and precise enough to correctly describe the flow (*i.e.* the distributions everywhere in the space domain). The bounds are given by a combination between the maximum macroscopic velocity and temperature of the flow ($\max_{\mathbf{x}}(u + c\sqrt{RT})$, where we take $c = 4$). The step of the grid is given by the smallest temperature (*i.e.* $\Delta v = \min_{\mathbf{x}} \sqrt{RT}$). These quantities are estimated here by the data, *e.g* velocity and temperature of the walls. Therefore, the velocity space is bounded to $[-v_{max}, v_{max}]^2$ with $v_{max} = 1731$ m.s^{-1}. The velocity grid is then a regular Cartesian grid with 40 points in v_x and v_y directions.

Finally, note that all the tests presented here have been computed on the SGI Altix 3700 of the scientific grouping CALMIP (see `http://www.calmip.cict.fr`). The algorithm presented in section 4 has been implemented by L. Mieussens in a code called CORBIS (COde Raréfié Bidimensionel Implicite Stationnaire) by using the language Fortran 90 and the shared memory parallel programming interface OpenMP. The total CPU time (sum of the CPU times used by each processor) for all the different simulations was between two hours for the smallest case to 300 hours for the largest one (pumping effect with 16 units). Generally, we only used six processors for the simulations.

5.2 Circulating flow

5.2.1 Ring-shaped channel

We first test the ring-shaped device described in figure 3, for which one unit as described in figure 2 is connected to its symmetric image. Due to this symmetry, the flow can be simulated in a single unit only, by using appropriate boundary conditions at the ends of the unit (see section 3.2).

We compute the steady flow for three different sizes of channel: thick ($\kappa = 1$), medium ($\kappa = 0.5$), thin ($\kappa = 0.1$), and for three different Knudsen numbers: $Kn = 1, 0.5, 0.1$. The channel is discretized with a number of cells that depends on its size: for the thick, medium, and thin channels we use respectively 400×96, 400×48, and 1600×24 cells. The first number is the number of cells along the curvilinear direction parallel to the boundary of the

channel, and the second one is the number of cells along the orthogonal direction. These grids have been chosen according to an accuracy study given at the end of this section.

In figures 7–9, we plot the non-dimensional velocity field $\frac{u}{\sqrt{2RT_L}}$ obtained at steady state (left plots). We also show a few streamlines plotted with the magnitude of the velocity field in gray scale (right plots). This allows to clearly see the movement of the gas. It appears that a circulating flow is well generated, at least for Knudsen numbers $Kn = 1$ and 0.5. The flow circulates in the direction of the temperature gradient of the circular part, and is therefore opposed to the direction of the temperature gradient of the straight part. This means that the thermal creep flow generated by the circular part is stronger than that created by the straight part. This last one remains confined close to the straight boundaries, while the main flow created by the circular part propagates in the whole channel. In other words, for $Kn = 1$ and 0.5, the flow is in the transition regime: the pressure driven flow spread over the whole channel, inducing a large velocity slip on the boundary. This velocity slip compensates or even dominates the thermal creep on the straight surface. Therefore, the thermal creep is invisible on the straight surface (top and middle plots of figures 7–9). This is due to the twofold effect of curvature, which, on one hand, increases the temperature gradient along the inner curved boundary and thus enhances the thermal creep there and, on the other, gives rise to a higher resistance for the pressure-driven flow in the curved channel. To sum up, the straight part plays the same role as the ditches of the device studied in [5, 43]. However, for $Kn = 0.1$, the flow is in the slip-flow regime: although the pressure driven flow is dominant in the middle of the straight channel, one observes the thermal creep on the straight surface (bottom plots of figures 7–9).

Also note that the flow is far from being uniform in the channel. We can observe some recirculation zones located at the beginning of the circular part, and the other one at the end of the straight part. The velocities in these zones are very weak, but they are also stronger as κ decreases (the channel becomes thiner and longer). Moreover, the recirculation zones enlarge as κ and Kn decrease. Note that the recirculation zones show inward and outward spiraling streamline patterns. This suggests that our results are not accurate enough in these zones (the velocity field is under-resolved). The reason is that the flow is very slow there (see the velocity scales in the figures), and hence can hardly be captured. Therefore the streamlines plotted in the recirculation zones give only approximate information about the structure of the flow.

Finally, for the smallest Knudsen number $Kn = 0.1$ it is not clear wether a global mass flow is really created along the channel. In the thick case (figure 7, bottom) there are very large recirculation zones, and in the medium thin cases (figures 8–9, bottom) the thermal creep flow generated by the straight part looks as strong as the one of the circular part. However, it can be noticed that the maximum velocities are still located close to the inner circular boundary.

Consequently, it seems more reliable to compute the average mass flow rate across a section of the channel to determine if there is or not a net mass flow created by our devices. Following [43, 5], we define the non-dimensionalized mass flow rate across a section Σ of the

channel by

$$\mathcal{M} = \frac{\int_{\Sigma} \rho \mathrm{u} \cdot \mathrm{n}\, d\Sigma}{\rho_{av}\sqrt{2RT_L}D},$$

where ρ_{av} is the average density in the channel. According to equations (3) or (9), this quantity must be constant along the channel. However, due to numerical errors, it presents some small fluctuations. Therefore, we compute an average of $\mathcal{M}$ along the channel, as well as its standard deviation from this average (this also gives a good accuracy test for our method). The results are plotted in figure 10 for the three different channels and for the three different Knudsen numbers. We observe that there is indeed a positive mass flow for every case, except for the thinest channel ($\kappa = 0.2$) with $Kn = 0.1$. In this case, the standard deviation is larger than the average value. This means that there is practically no net mass flow in the device, or at least it is too small to be captured by our computation.

5.2.2 Accuracy of the computations

The accuracy of our computations has been studied by using three different grids for each geometry: a coarse mesh, a fine mesh, and a very fine mesh. Each mesh has twice as many cells as the coarser mesh in each direction.

For instance for the thick channel with $Kn = 1$, we used 100×24, 200×48, and then 400×96 cells. First we compared the values obtained for the density profiles averaged in the section of the channel. We found that the difference between the coarse and the very fine meshes is less than 1.3 %, while the difference between the fine and the very fine meshes is less than 0.3 %. This means that the coarse mesh is accurate enough to accurately capture the macroscopic profiles. We also compared the values obtained for the mass flow rate across a section. For this quantity, the standard deviation from the average value is a good test of accuracy. We found 4 % for the coarse mesh, 1 % for the fine mesh, and then 0.2 % for the very fine mesh. Consequently, since the mass flow rate is the most important quantity to be computed in this section, we used the very fine mesh for this case.

The same analysis has been carried out for the other Knudsen numbers, and for the medium and thin channels. The density profiles can be computed with the coarse mesh up to 2 % of accuracy as compared to the very fine mesh. To compute the mass flow rate, the very fine grid must be used, but the standard deviation reaches up to 6 % for the medium channel with $Kn = 0.5$. Note that for the thin channel, as previously mentioned, the circulating flow effect seems to be so small for $Kn = 0.1$ that we were not able to correctly compute the mass flow rate, even with the very fine mesh (1600×24 cells).

It is known that the velocity distribution function possesses a discontinuity in the gas around a convex body [36, 42, 37], and this fact applies to the present problem. That is, the inner curved boundary produces a discontinuity in F in the velocity space. It should be mentioned, however, that the present numerical method, which is quite flexible concerning the geometry, is not designed to describe the discontinuity. For accurate numerical treatment of the discontinuity produced by a convex body, the reader is referred to for instance [4, 42, 44, 40, 45]. Below, we investigate the effects of the velocity grid on the simulations.

For the thick channel with $Kn = 1$, and a space grid of 400×96 cells, we compared the results obtained for three different velocity steps $\Delta v = 2\sqrt{RT_L}/a$ with $a = 5, 10, 20$, and three different velocity bounds given by $v_{max} = c\sqrt{RT_H}$ with $c = 2, 4, 8$. The number of velocities then varies from 10×10 to 180×180. The velocity grid $(c = 4, a = 20)$ is considered as the reference solution in these comparisons (the finest grid $(c = 8, a = 20)$ is too computationally expensive). In table 1, according to the discussion at the end of section 5.2.1, we give the average mass flux along the channel, as well as its standard deviation from the average. It appears that the average is wrong for small bounds $(c = 2)$. The grid $(c = 4, a = 10)$ can be considered as sufficiently fine, since the average mass flux is different from the reference value by less than 5 %, and its standard deviation is less than 0.3 %. Increasing the bounds does not increase the accuracy. In table 2, we give the maximum pointwise relative difference (in %) of the density and the horizontal velocity, computed in the whole space domain, with respect to the reference solution. For the density, the grid $(c = 4, a = 10)$ is again sufficiently accurate (the same results have been obtained for the temperature and pressure). For the horizontal velocity, this grid gives a difference of around 28%, which is quite large. However, this large difference is located in very small zones, and does not seem to propagate outside these zones. Since we are mainly interested in the pressure and density profile in our tests, the grid $(c = 4, a = 10)$ is sufficiently fine to be used in the remainder of this paper.

5.2.3 Infinite cascade of S-shaped channels

For this test—corresponding to the device presented in figure 4—we also simulate the flow in a single unit by changing the periodic boundary conditions (see section 3.2). We observed that the results are almost the same as for the ring-shaped channel: the same mass flow rate and the same average macroscopic profiles are obtained. The only difference is the direction of the velocity field at the junction between the straight and circular parts. A comparison of the two systems (closed ring and infinite cascade) is given in figure 11 for the case $\kappa = 1$ and $Kn = 1$: we plot the velocity field in the whole ring (top) and in one period of the cascade. Note that these picture are not the result of a computation in the full domain but are in fact obtained by symmetry from computations in a single unit only.

5.3 Pumping effect

Now we test the device presented in figure 5 where the channel of N units is closed at both ends. We define the non-dimensionalized average pressure and density in a section Σ of the channel by

$$P(s) = \frac{\int_{\Sigma(s)} p \, d\Sigma(s)}{D\rho_{av}RT_L}, \qquad R(s) = \frac{\int_{\Sigma(s)} \rho \, d\Sigma(s)}{D\rho_{av}}, \tag{30}$$

where s is a curvilinear abscissa given by the length of the median curve of the channel. Note that s varies between 0 and $L = 2NL_S$.

The size of this unit is given by $\kappa = 0.5$ (thick case), and the Knudsen number is set to 0.5. Our simulations are made for the following number of units: $N = 2, 4, 8, 16$. Since

we are interested in average macroscopic quantities only, a coarse mesh as defined in the previous section is sufficient (see the end of section 5.2.1). Consequently, we use a mesh of 100×24 cells per unit (we remind that for this mesh with a single unit in the circulating flow test, the density profile is the same as the profile computed with a very fine mesh of 400×96 cells, up to an error of 1.5 %).

We plot in figure 12 the average pressure and density profiles as functions of s as defined in (30), as well as their average values in each unit. Although these profiles oscillate with the same frequency as the wall temperature (lines with symbols), they are globally affine functions of the length of the channel. More precisely, if we look at the average of these profiles in each unit and then link each averaged values, we obtain curves that are close to straight lines (the dotted lines in figure 12). This may give an easy estimation of the pressure gain that could be obtained with a larger number of units. However, note that for 16 units, this curve is slightly convex (especially for the pressure profile). This means that the pressure gain may be smaller than expected. This is discussed below.

We also plot in figure 13 the pressure and density gains (in percent) defined as

$$\frac{P(0) - P(L)}{P(L)} \times 100, \qquad \frac{R(0) - R(L)}{R(L)} \times 100. \tag{31}$$

We observe that these gains are almost 50% for 16 units and that they look as affine functions of the number of units. If we extrapolate the line obtained with 2,4,8 and 16 units, we find that a gain of 100% could be obtained with 32 or 36 units. This is of course a rough estimation. As noted below, it is possible that this gain is actually smaller than expected, mainly for the following reason. Indeed as the density increases at one end of the channel, the local Knudsen number decreases and the gas becomes more and more dense. According to the kinetic theory, the thermal creep flow should be less and less strong. Consequently, the pumping effect should be weaker and weaker as well. This fact is already visible in figure 12 on the pressure profile.

A two dimensional picture of the macroscopic quantities in the 16 unit device can be viewed in figure 14. The periodic temperature field is clearly visible, as well as the increase of the density and pressure values along the channel. There is almost no variation of these three fields along the transverse direction. The velocity field has a more complex structure, but its magnitude is rather small.

5.4   A comparison with the true Boltzmann model

It is generally admitted that the BGK model is physically correct only for flows that are close to equilibrium. This belief relies on the facts that the structure of the BGK collision operator is very simple as compared to the real Boltzmann equation, while it gives the same fluid equations for small Knudsen numbers. However, it is a model for any deviation from a local equilibrium designed in such a way that it satisfies basic properties of the Boltzmann equation, and for some cases, it turns out that the BGK model is able to give precise results

that are quantitatively very close to that of the Boltzmann model, even for intermediate Knudsen numbers. This is in particular true in our study, as it is shown in the following.

We use the test of section 5.3 to compare the BGK and Boltzmann models. The Boltzmann equation is solved with the classical Direct Simulation Monte-Carlo (DSMC) method (see [9]; the computation was carried out by H. Yoshida basically using the code developed in [2]). The parameters of the DSMC computation are the followings: the number of cells is 4000 for each unit (that is 1.7 times as many cells as in our BGK computations); the total number of particles is 200,000 per unit, thus averaged number of particles per cell is 50; the time step Δt is $2t_0/\sqrt{\pi} \times 10^{-2}$, where $t_0 = (\sqrt{\pi}/2)(2RT_0)^{-1/2}l_0$ is the mean free time corresponding to l_0(mean free path), which gives $\Delta t \approx 10^{-5}$. The longest case took more than 6,000,000 steps to reach the steady state while the other cases took about 3,000,000 steps. In order to get the time-averaged steady state profile (so as to reduce the statistical noise), 1,000,000 steps more are needed. Note that for DSMC the hard-sphere model is used, hence the definition of the Knudsen number is not given by (29) but rather by $Kn = \frac{l_0}{D}$ with $l_0 = \frac{m}{\sqrt{2}\pi d_m^2 \rho_0}$ and d_m is the diameter of the molecules (see [43]). Finally, we mention that the DSMC code is implemented with Fortran 90 and is parallelized with MPI.

We plot the non-dimensional average pressure obtained in pumping devices of 1, 2, 4, and 8 units with both the BGK and Boltzmann models (figure 15). It clearly appears with this figure that the two models are very close for 2 to 8 units. More precisely, the maximum relative difference is found to be lower than 1.7 %. For the 1 unit device, the difference is larger, since the maximum relative difference is 5.2 %.

This clearly demonstrates that the BGK model is accurate enough to describe the flows considered in this study, at least if one is only interested in the average macroscopic quantities as the pressure. It is likely that more fine comparisons, like velocity field at the boundary for instance, would show larger differences between BGK and DSMC. In this case, it may be tried to modify the relaxation time so as to match the heat conductivity instead of the viscosity, or rather to use the Ellipsoidal-Statistical BGK (ES-BGK) model [18]. This model allows to get the correct Prandtl number, that is to say to match both the viscosity and heat conductivity coefficients. While these models have not been tested in this manuscript, this should not be a difficult issue: indeed, the code CORBIS used in this work could easily be modified, since it is based on an algorithm that is able to treat the ES-BGK model, see [27].

Even if the two methods have not been used on the same computer, we give below a rough comparison on the CPU time consumed for the 8 unit case: the DSMC computation required around 15 days with 8 processors Pentium IV (2.4 Ghz) for a total time of 4 months, while our BGK computation required only 1 day and a half with 6 processors Itanium II (1.5 Ghz) of the SGI Altix 3700, for a total time of 7 days. The main reason for the very large CPU time of the DSMC computation is that, due to the long size of the channel, the steady state is reached after a very long physical time. Note that this comparison probably over-estimates the performance of our BGK code, since it is well known that Itanium II is faster than Pentium IV for scientific computing (see, for instance, http://www.netlib.org/benchmark/performance.ps).

5.5 Efficiency of the implicit boundary conditions

Here the performance of the implicit treatment of the boundary conditions (see section 4.4) is shown for the pumping device with 8 and 16 units.

For this case, we plot the residual histories at the top of figure 16 for our linearized implicit scheme used with explicit and implicit boundary conditions. We observe that the scheme with implicit B.C converges faster: it requires 900 iterations while the scheme with explicit B.C converges in 1250 iterations. The speed of convergence is thus increased by a factor of 40% for this test case.

For the 16 unit case, the same comparison has not been performed completely, since the computation is very long with explicit B.C. However, it seems that the performance of the implicit B.C is enhanced for this case, as it can be seen at the bottom of figure 16, even if the computation with explicit B.C has not been carried at convergence. Indeed, the linear profile of the residual suggests that the number of iterations to reach the steady state would be around 6500 with the explicit B.C, while with the implicit B.C the algorithm only needs 2200 iterations (which is therefore 3 times as fast in this case).

Consequently, the implicit treatment of the B.C seems to speed up the convergence of our scheme, as well as its scalability. However, the convergence is still globally linear (after the rapid decreasing between 0 and 100 iterations), and the scalability is still not very good, since the number of iterations to reach the steady state seems to be a highly increasing function of the number of units: for 1, 2, 4, 8, and 16 units, the number of iterations is respectively 100, 127, 267, 732, and 2272.

It is therefore difficult to compute a flow for a device with more than 32 units with this algorithm. We hope that a more sophisticated linear solver could further improve this convergence. However, for very long devices, we have proposed an alternative strategy presented in [3] which consists in using an asymptotic model for the thin channel approximation. This allows to compute macroscopic profiles with an arbitrary large number of units very rapidly.

6 Conclusion

In this paper, we have presented a system of Knudsen pump in a channel that works without moving part for a gas under rarefied conditions or in micro-scales. Our device is based both on the thermal creep effect and on a varying curvature of the channel that makes the system very simple.

A numerical method has been proposed to simulate the pump. This method—while it is based on a simplified kinetic model—turns out to be very efficient and gives results that are very close to what can be obtained by a classical DSMC, for a small computational time. As compared to other numerical methods for the BGK equation (such as in [4]), our method is not restricted to rectangular Cartesian grids. Our numerical tests demonstrate that a circulating flow can be controlled in our device, as well as a non negligible pressure ratio in case of a cascade of several units closed at both ends.

We hope that this system could be efficiently used on MEMS. Now it should be necessary

to make an intensive optimization study in order to determine the optimal parameters of our device, so as to maximize the compression ratio. We believe that our numerical method is an efficient tool for such a study.

We also mention that this new device is the core of a large project in which we also have investigated the applicability of simpler macroscopic fluid models derived from kinetic theory by means of asymptotic methods (see [24] for a fluid-dynamic model for small Knudsen numbers and [3] for a simple one dimensional diffusion model). The present study is also a relevant way to validate these fluid models.

However, for a practical application of our device, it should be equally (or even more) important to use a pipe instead of a plane channel. The behavior of the device may be slightly different in this case, since, as it has been noted in [5], the pipe resistance to the pressure is larger than that of a plane channel. This results in a device with a weaker flow, but a stronger compression ratio. But for such a system, full three dimensional computations are necessary, which—for long pipes—requires at present prohibitively large computational times when using kinetic simulations. Therefore, as a preliminary study, it is very useful to use fast kinetic simulations of a 2D plane device.

From the point of view of engineering, it might be very difficult to maintain a temperature gradient as strong as it is in this study ($T_H/T_L = 3$). However, this gradient was mainly used to make the computation easier, since it allows to exaggerate the flow. Indeed, the typical normalized flow speed (which is more or less the typical Mach number) is 0.005 in figure 7, for instance. This shows that if our device could be used in a room with standard ambient pressure and temperature, the flow speed could be more than 1m/sec, which is quite large. Consequently, even if the imposed temperature difference is small, say, $T_H = 440K$ and $T_L = 400K$ ($T_H/T_L = 1.1$), one can still expect a flow of a few centimeters per second, which is of practical level in microscale applications. There is no technical problem to maintain such a small temperature difference in microscale devices. Finally, we should also note that in macroscale applications for vacuum technology, it is possible to realize the large temperature ratio by cooling.

Acknowledgments

References

[1] A. A. Alexeenko, S. F. Gimelshein, E. P. Muntz, and A. D. Ketsdever. Kinetic modeling of temperature driven flows in short microchannels. *International Journal of Thermal Sciences*, 45(11):1045 – 1051, 2006.

[2] K. Aoki, P. Degond, L. Mieussens, M. Nishioka, and S. Takata. In M. S. Ivanov and A. K. Rebrov, editors, *Rarefied Gas Dynamics*, pages 1079–1084. Siberian Branch of the Russian Academy of Sciences, Novosibirsk, 2007.

[3] K. Aoki, P. Degond, L. Mieussens, S. Takata, and H. Yoshida. A diffusion model for rarefied flows in curved channels. *Multiscale Model. Simul.*, 6(4):1281–1316, 2007.

[4] K. Aoki, K. Kanba, and S. Takata. Numerical Analysis of a Supersonic Rarefied Gas Flow Past a Flat Plate. *Phys. Fluids*, 9(4), 1997.

[5] K. Aoki, Y. Sone, S. Takata, K. Takahashi, and G. A. Bird. One-way flow of a rarefied gas induced in a circular pipe with a periodic temperature distribution. In Timothy J. Bartel and Michael A. Gallis, editors, *Rarefied gas dynamics, Vol 1: 22nd International Symposium*, volume 585, pages 940–947. AIP, 2001.

[6] V. V. Aristov. *Direct methods for solving the Boltzmann equation and study of nonequilibrium flows*, volume 60 of *Fluid Mechanics and its Applications*. Kluwer Academic Publishers, Dordrecht, 2001.

[7] P.L. Bhatnagar, E.P. Gross, and M. Krook. A model for collision processes in gases. I. small amplitude processes in charged and neutral one-component systems. *Phys. Rev.*, 94:511–525, 1954.

[8] J. R. Bielenberg and G. H. Brenner. A continuum model of thermal transpiration. *J. Fluid Mech.*, 546:1–23, 2006.

[9] G.A. Bird. *Molecular Gas Dynamics and the Direct Simulation of Gas Flows*. Oxford Science Publications, 1994.

[10] A. V. Bobylev and S. Rjasanow. Fast deterministic method of solving the Boltzmann equation for hard spheres. *Eur. J. Mech. B Fluids*, 18(5):869–887, 1999.

[11] C. Buet. A Discrete-Velocity Scheme for the Boltzmann Operator of Rarefied Gas Dynamics. *Transp. Th. Stat. Phys.*, 25(1):33–60, 1996.

[12] C. Cercignani. *The Boltzmann Equation and Its Applications*, volume 68. Springer-Verlag, Lectures Series in Mathematics, 1988.

[13] C. Cercignani. *Slow rarefied flows: Theory and application to micro-electro-mechanical systems*, volume 41 of *Progress in Mathematical Physics*. Birkhäuser Verlag, Basel, 2006.

[14] B. Dubroca and L. Mieussens. A conservative and entropic discrete-velocity model for rarefied polyatomic gases. In *CEMRACS 1999 (Orsay)*, volume 10 of *ESAIM Proc.*, pages 127–139 (electronic). Soc. Math. Appl. Indust., Paris, 1999.

[15] F. Filbet, C. Mouhot, and L. Pareschi. Solving the Boltzmann equation in $N \log_2 N$. *SIAM J. Sci. Comput.*, 28(3):1029–1053 (electronic), 2006.

[16] V. Garzó and A. Santos. Comparison Between the Boltzmann and BGK Equations for Uniform Shear Flows. *Physica A*, 213:426–434, 1995.

[17] Y. L. Han, M. Young, E. P. Muntz, and G. Shiflett. Knudsen compressor performance at low pressures. In M. Capitelli, editor, *Rarefied gas dynamics*, pages 162–167. AIP, 2005.

[18] L. H. Holway. Kinetic theory of shock structure using an ellipsoidal distribution function. In New York Academic Press, editor, *Rarefied Gas Dynamics, Vol. 1 (Proc. Fourth Internat. Sympos. Univ. Toronto, 1964)*, pages 193–215, 1966.

[19] A. B. Huang and P. F. Hwang. Test of statistical models for gases with and without internal energy states. *Physics of Fluids*, 16(4):466–475, 1973.

[20] M. L. Hudson and T. J. Bartel. DSMC simulation of thermal transpiration and accomodation pump. In R. Brun, R. Campargue, R. Gatignol, and J.-C. Lengrand, editors, *Rarefied Gas Dynamics, Vol 1*, pages 719–726. CEPADUES, Toulouse, 1999.

[21] G. Karniadakis, A. Beskok, and N. Aluru. *Microflows and nanoflows: Fundamentals and simulation*, volume 29 of *Interdisciplinary Applied Mathematics*. Springer, New York, 2005.

[22] M. Knudsen. Eine revision der gleichgewichtsbedingung der gase. *Annalen der Physik*, 336(1):205–229, 1909.

[23] M. Knudsen. Thermischer molekulardruck der gase in röhren. *Annalen der Physik*, 338(16):1435–1448, 1910.

[24] C. J. T. Laneryd, K. Aoki, P. Degond, and L. Mieussens. Thermal creep of a slightly rarefied gas through a channel with curved boundary. In 25st *RGD Symposium, Book of Abstracts*, St-Petersburg, 2006.

[25] J. C. Maxwell. On stresses in rarified gases arising from inequalities of temperature. *Philosophical Transactions of the Royal Society of London*, 170:231–256, 1879.

[26] L. Mieussens. Discrete Velocity Model and Implicit Scheme for the BGK Equation of Rarefied Gas Dynamics. *Math. Models and Meth. in Appl. Sci.*, 8(10):1121–1149, 2000.

[27] L. Mieussens. Discrete-velocity models and numerical schemes for the Boltzmann-BGK equation in plane and axisymmetric geometries. *J. Comput. Phys.*, 162:429–466, 2000.

[28] L. Mieussens. Convergence of a discrete-velocity model for the Boltzmann-BGK equation. *Comput. Math. Appl.*, 41(1-2):83–96, 2001.

[29] T. Ohwada. Structure of normal shock waves: direct numerical analysis of the Boltzmann equation for hard-sphere molecules. *Phys. Fluids A*, 5(1):217–234, 1993.

[30] T. Ohwada, Y. Sone, and K. Aoki. Numerical analysis of the shear and thermal creep flows of a rarefied gas over a plane wall on the basis of the linearized boltzmann equation for hard-sphere molecules. *Phys. Fluids A*, 1:1588–1599, 1989.

[31] G. Pham-Van-Diep, P. Keeley, E. P. Muntz, and D. P. Weaver. A micromechanical Knudsen compressor. In J. Harvey and G. Lords, editors, *Rarefied gas dynamics*, volume 1, pages 715–721. Oxford University Press, 1995.

[32] O. Reynolds. On certain dimensional properties of matter in the gaseous state. Part I and II. *Philosophical Transactions of the Royal Society of London*, 170:727–845, 1879.

[33] F. Rogier and J. Schneider. A Direct Method For Solving the Boltzmann Equation. *Transp. Th. Stat. Phys.*, 23(1-3):313–338, 1994.

[34] Y. Sone. Thermal creep in rarefied gas. *J. Phys. Soc. Jpn*, 21:1836–1837, 1966.

[35] Y. Sone. Flows induced by temperature fields in a rarefied gas and their ghost effect on the behavior of a gas in the continuum limit. volume 32 of *Annu. Rev. Fluid Mech.*, pages 779–811. Annual Reviews, Palo Alto, CA, 2000.

[36] Y. Sone. *Kinetic theory and fluid dynamics*. Modeling and Simulation in Science, Engineering and Technology. Birkhäuser Boston Inc., Boston, MA, 2002.

[37] Y. Sone. *Molecular gas dynamics: Theory, techniques, and applications*. Modeling and Simulation in Science, Engineering and Technology. Birkhäuser Boston Inc., Boston, MA, 2007.

[38] Y. Sone, K. Aoki, and H. Sugimoto. The Bénard problem for a rarefied gas: formation of steady flow patterns and stability of array of rolls. *Phys. Fluids*, 9(12):3898–3914, 1997.

[39] Y. Sone and K. Sato. Demonstration of a one-way flow of a rarefied gas induced through a pipe without average pressure and temperature gradients. *Physics of Fluids*, 12(7):1864–1868, 2000.

[40] Y. Sone and H. Sugimoto. Kinetic theory analysis of steady evaporating flows from a spherical condensed phase into a vacuum. *Physics of Fluids A: Fluid Dynamics*, 5(6):1491–1511, 1993.

[41] Y. Sone and H. Sugimoto. Vacuum pump without a moving part and its performance. In E. P. Muntz and A. Ketsdever, editors, *Rarefied gas dynamics*, pages 1041–1046. AIP, 2003.

[42] Y. Sone and S. Takata. Discontinuity of the velocity distribution function in a rarefied gas around a convex body and the slayer at the bottom of the Knudsen layer. *Transport Theory Statist. Phys.*, 21(4–6):501–530, 1992.

[43] Y. Sone, Y. Waniguchi, and K. Aoki. One-way flow of a rarefied gas induced in a channel with a periodic temperature distribution. *Physics of Fluids*, 8(8):2227–2235, 1996.

[44] H. Sugimoto and Y. Sone. Numerical analysis of steady flows of a gas evaporating from its cylindrical condensed phase on the basis of kinetic theory. *Physics of Fluids A: Fluid Dynamics*, 4(2):419–440, 1992.

[45] S. Takata, Y. Sone, and K. Aoki. Numerical analysis of a uniform flow of a rarefied gas past a sphere on the basis of the boltzmann equation for hard-sphere molecules. *Physics of Fluids A: Fluid Dynamics*, 5(3):716–737, 1993.

[46] S. E. Vargo and E. P. Muntz. Initial results from the first MEMS fabricated thermal transpiration-driven vacuum pump. In Timothy J. Bartel and Michael A. Gallis, editors, *Rarefied gas dynamics, Vol 1: 22nd International Symposium*, volume 585, pages 502–509. AIP, 2001.

[47] P. Welander. On the temperature jump in a rarefied gas. *Arkiv für Fysik*, 7(44):507–553, 1954.

[48] J.Y. Yang and J.C. Huang. Rarefied Flow Computations Using Nonlinear Model Boltzmann Equations. *Journal of Computational Physics*, 120:323–339, 1995.

A   Jacobian matrices of the Maxwellian mappings $\vec{\rho} \mapsto M_{\mathrm{k}}[\vec{\rho}]$ and $\vec{\rho} \mapsto N_{\mathrm{k}}[\vec{\rho}]$

Elementary calculus gives the following formulae:

$$\partial_{\vec{\rho}} M_{\mathrm{k}}[\vec{\rho}] = M_{\mathrm{k}}[\vec{\rho}]\vec{m}(\mathrm{v_k})^T A(\vec{\rho})^{-1}$$

$$\partial_{\vec{\rho}} N_{\mathrm{k}}[\vec{\rho}] = N_{\mathrm{k}}[\vec{\rho}](\vec{m}(\mathrm{v_k}) - \frac{1}{\alpha_4(\vec{\rho})}\vec{e})^T A(\vec{\rho})^{-1},$$

where $A(\vec{\rho})$ is the following 4×4 matrix

$$A(\vec{\rho}) = \sum_{\mathrm{k}} \left(\vec{m}(\mathrm{v_k})\vec{m}(\mathrm{v_k})^T M_{\mathrm{k}}[\vec{\rho}] + \vec{e}\left(\vec{m}(\mathrm{v_k}) - \frac{1}{\alpha_4(\vec{\rho})}\vec{e}\right)^T N_{\mathrm{k}}[\vec{\rho}] \right) \Delta \mathrm{v}.$$

B   Diagonal of the relaxation matrix R^n

Using the relations given in appendix A, the first half of this diagonal—related the 2×2 block structure of R^n—is

$$\Delta_{i,j,\mathrm{k}}^n = \frac{1}{\tau_{i,j}^n} \left(M_{\mathrm{k}}[\vec{\rho}_{i,j}^n]\vec{m}(\mathrm{v_k})^T A(\vec{\rho}_{i,j}^n)^{-1}\vec{m}(\mathrm{v_k})\Delta \mathrm{v} - 1 \right),$$

while the second half is

$$\Delta_{i,j,\mathrm{k}}^n = \frac{1}{\tau_{i,j}^n} \left(N_{\mathrm{k}}[\vec{\rho}_{i,j}^n]\left(\vec{m}(\mathrm{v_k}) - \frac{1}{\alpha_4(\vec{\rho}_{i,j}^n)}\vec{e}\right)^T A(\vec{\rho}_{i,j}^n)^{-1}\vec{e}\Delta \mathrm{v} - 1 \right).$$

low temperature T_L high temperature T_H

momentum transfered by the molecules to the wall

A

momentum
of hot molecule

momentum
of cold molecules
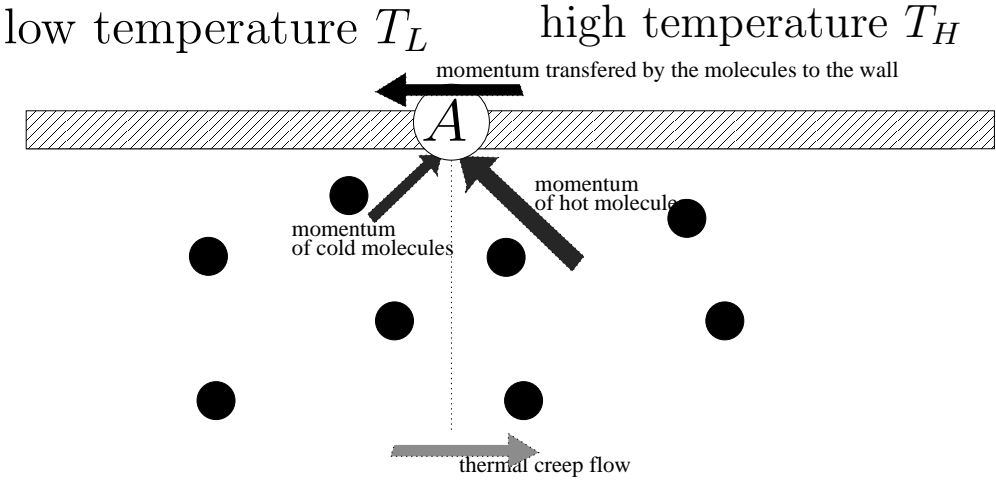
thermal creep flow

Figure 1: Physical mechanism of the thermal creep flow: the average momentum transferred to the boundary by the molecules coming from the right to point A (large black arrow) is larger than that transferred by molecules coming from the left (small black arrow). This results in a net momentum transferred to the boundary directed from the right to the left (horizontal black arrow). By reaction, the wall makes the gas move from the left to the right (gray arrow).
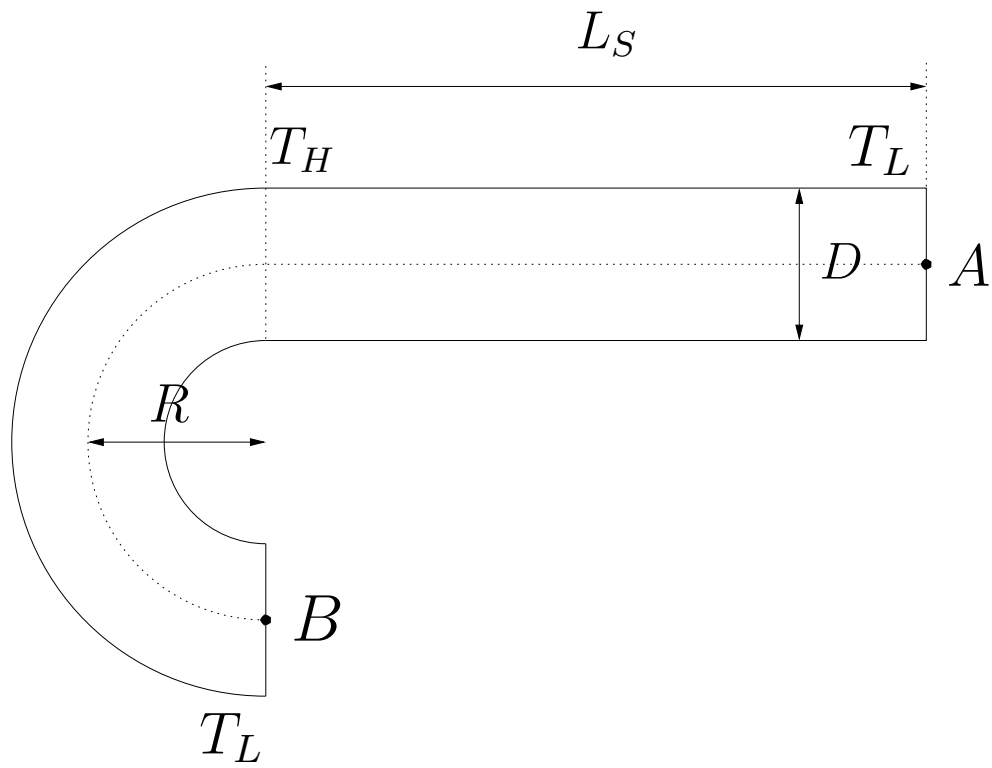
Figure 2: Basic unit of our devices : a hook shaped channel.
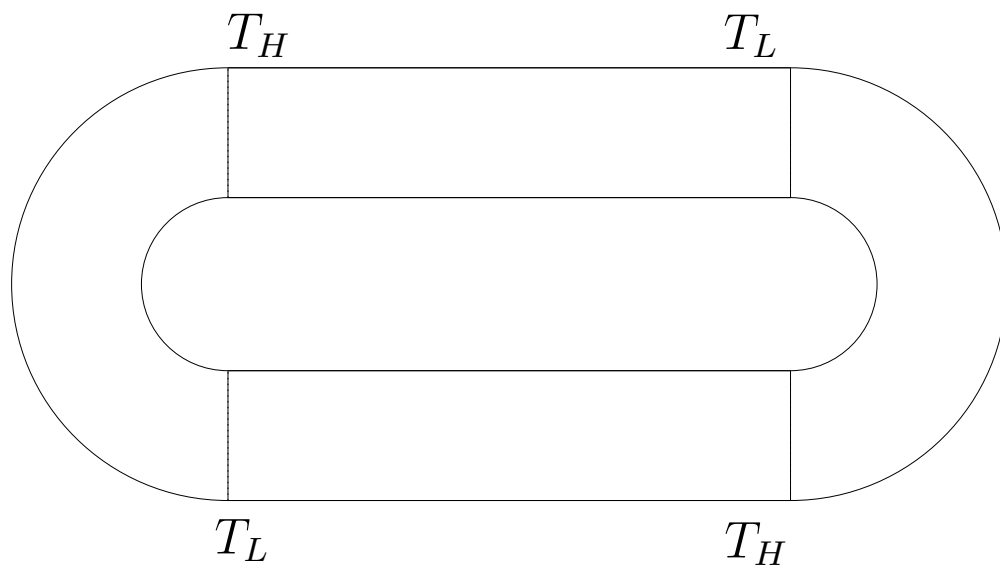
Figure 3: Ring shaped channel to generate a circulating flow.
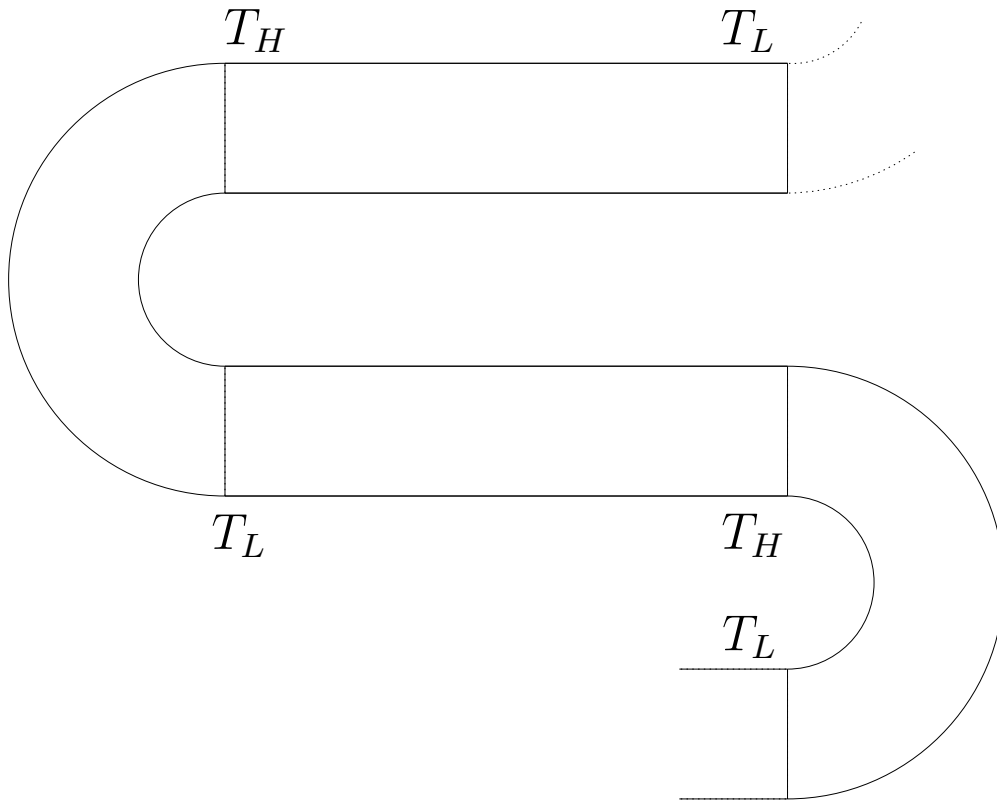
Figure 4: S shaped channel to generate a one-way flow in an infinite cascade.
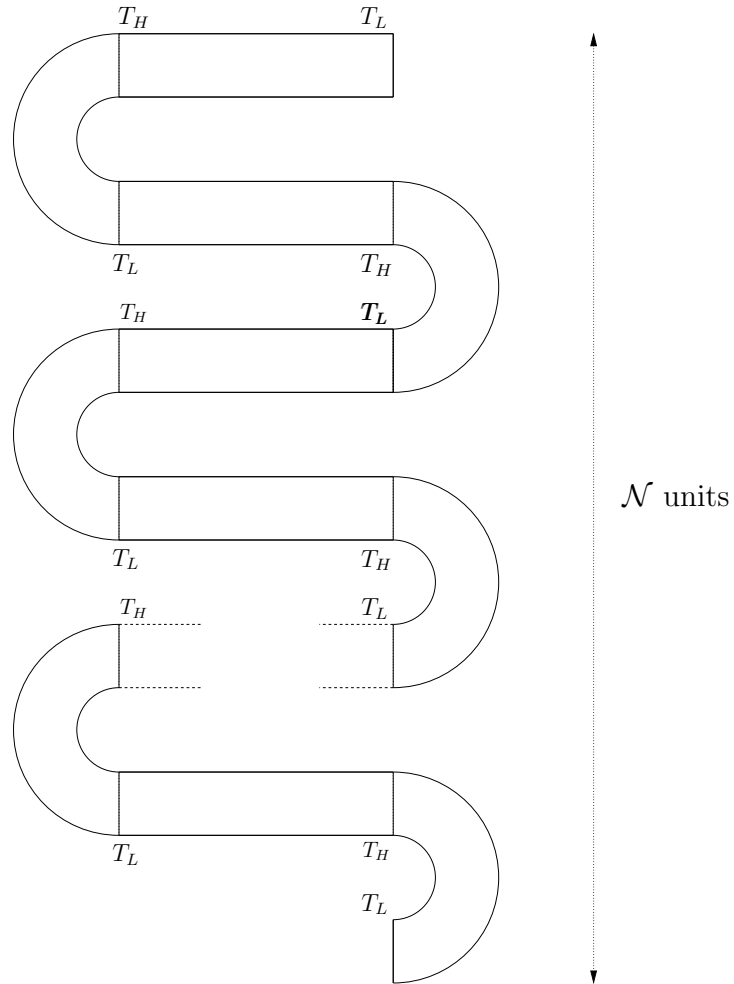
Figure 5: Closed cascade device to generate a pumping effect.
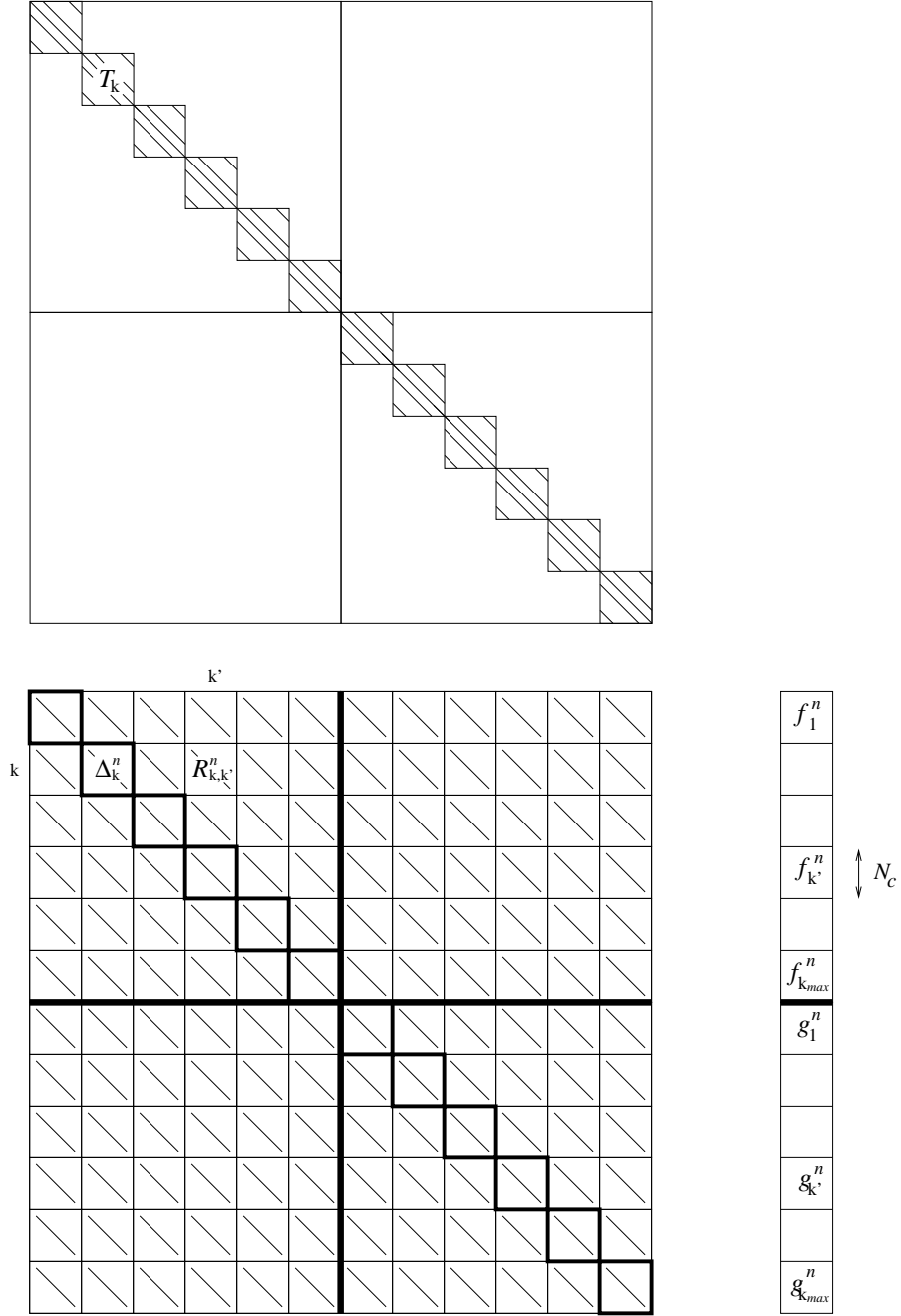
Figure 6: Block (sparse) structure of the matrices of the linearized implicit scheme (22): T (top), R^n with its diagonal sub-blocks Δ_k^n (bottom left), and the corresponding unknown vector $U^n = (f^n, g^n)$ (bottom right).
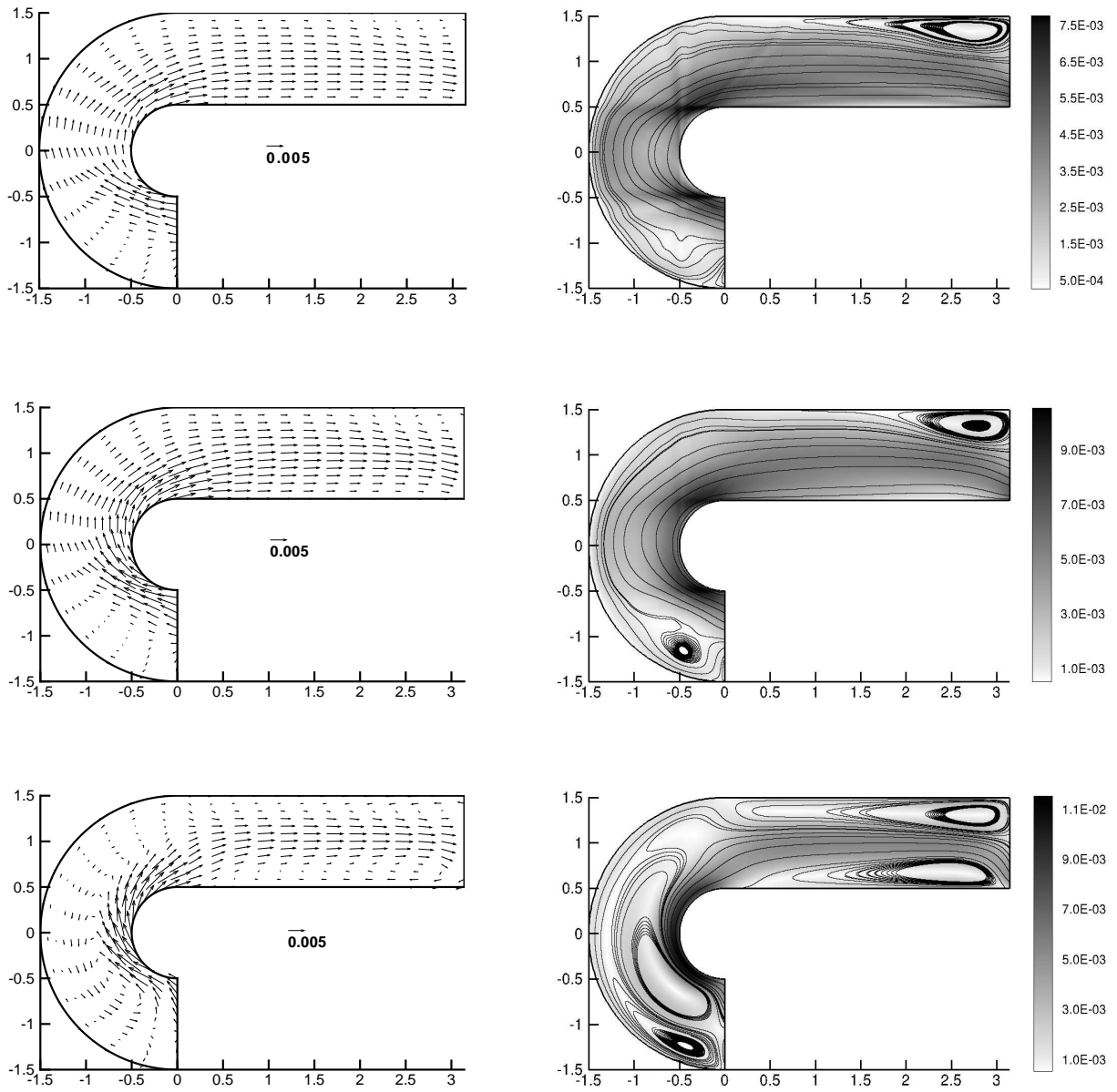
Figure 7: Non-dimensional velocity fields $\frac{u}{\sqrt{2RT_L}}$ (left) and streamlines (right) with magnitude of the velocity in gray scale in half of the ring-shaped channel. The non-dimensional vector field scale is shown with the arrow and the corresponding numeric value printed below it (left). Thick case ($\kappa = 1$) with $Kn = 1$ (top), $Kn = 0.5$ (middle), and $Kn = 0.1$ (bottom).
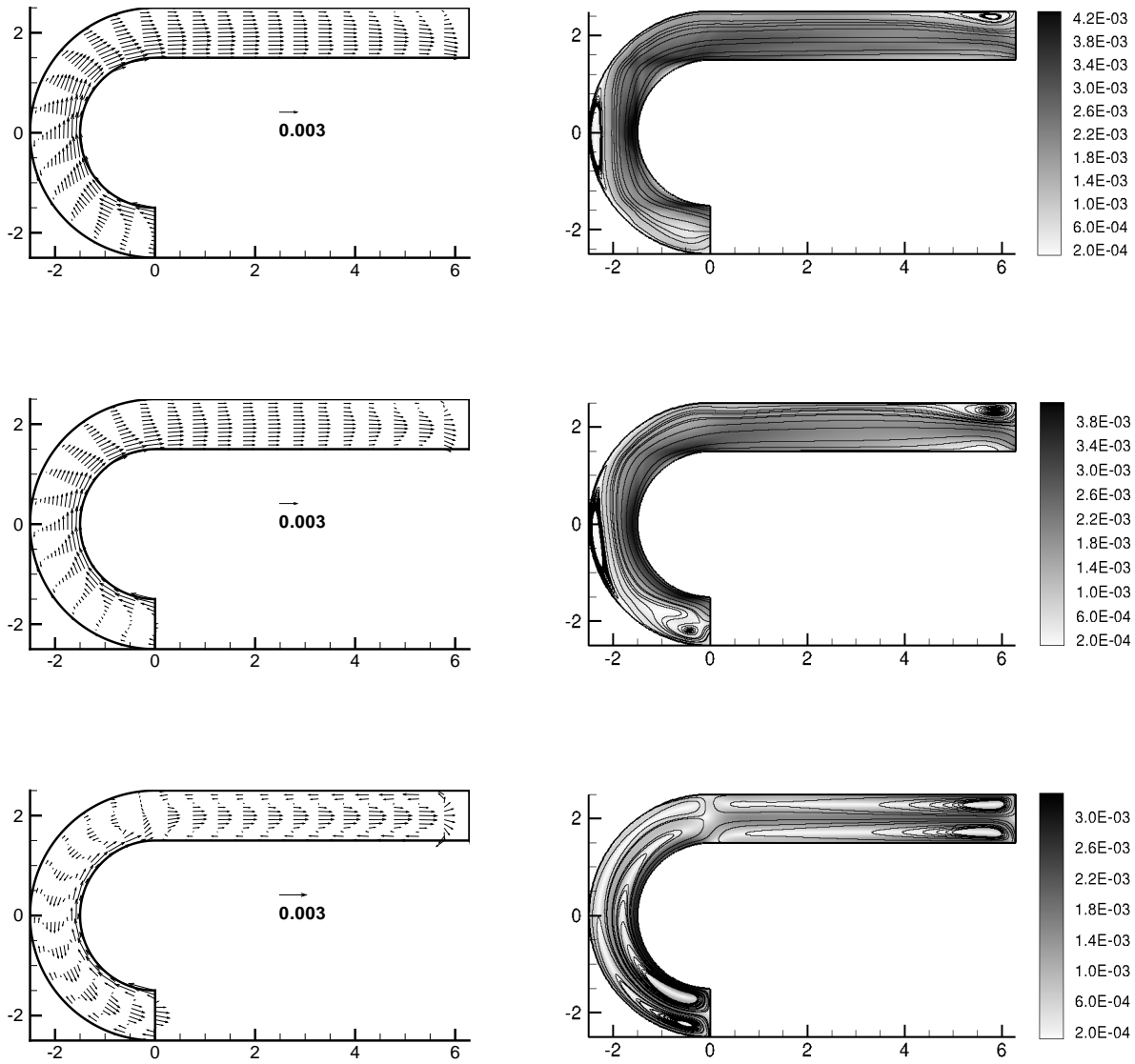
Figure 8: Same as figure 7 for the medium case ($\kappa = 0.5$).
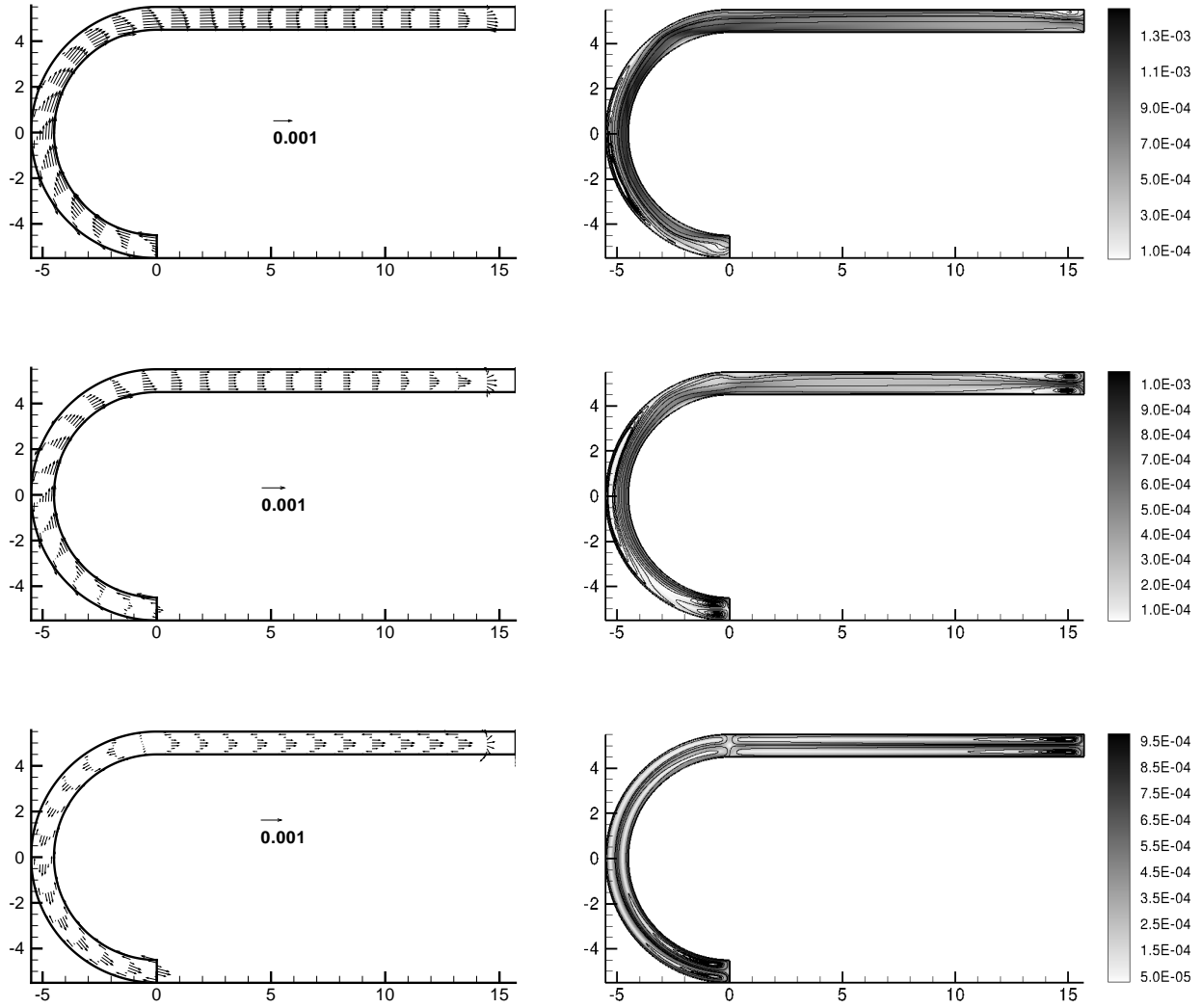
Figure 9: Same as figure 7 for the thin case ($\kappa = 0.1$).
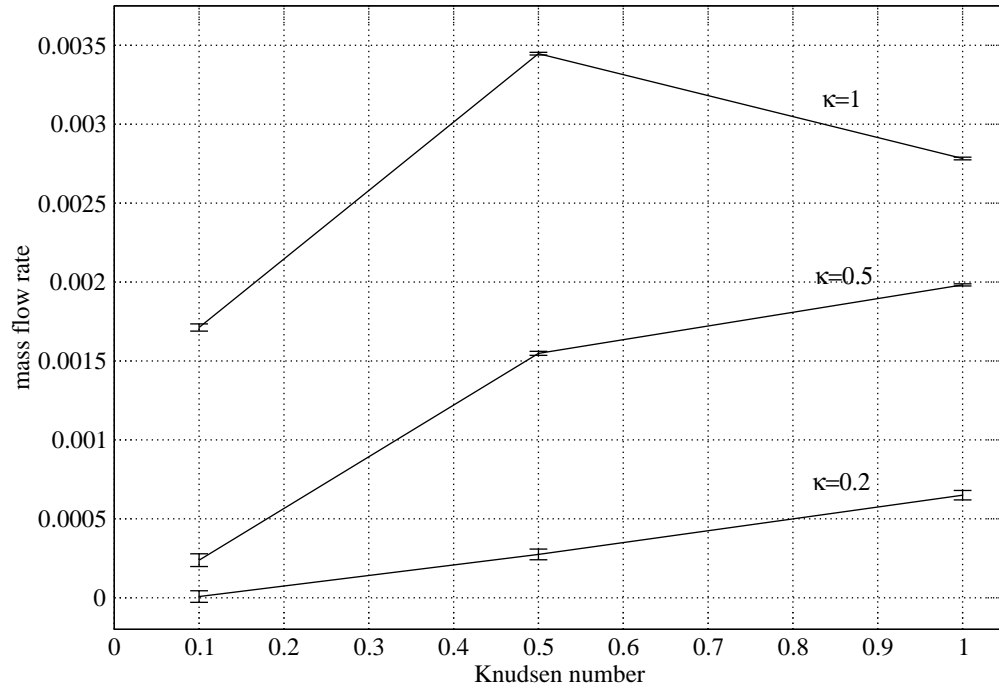
Figure 10: Averaged values of the mass flow rate in the ring-shaped channel as a function of the Knudsen number. Each curve corresponds to one of the three different channel (thick $\kappa = 1$, medium $\kappa = 0.5$, and thin $\kappa = 0.2$). The horizontal bars represent the standard deviation of the mass flow rate from its average.

	$c = 2$	$c = 4$	$c = 8$
$a = 5$	$-1.693 \times 10^{-4} \pm 5.2\%$	$2.308 \times 10^{-3} \pm 0.4\%$	$2.311 \times 10^{-3} \pm 0.4\%$
$a = 10$	$-1.940 \times 10^{-4} \pm 4.0\%$	$2.783 \times 10^{-3} \pm 0.3\%$	$2.787 \times 10^{-3} \pm 0.3\%$
$a = 20$	$-3.267 \times 10^{-4} \pm 2.4\%$	$2.910 \times 10^{-3} \pm 0.3\%$	

Table 1: Average of the mass flux along the ring-shaped channel and its standard deviation (in %) for velocity grids with three different steps $\Delta v = 2\sqrt{RT_L}/a$ with $a = 5, 10, 20$ and three different bounds given by $v_{max} = c\sqrt{RT_H}$ with $c = 2, 4, 8$.

	$c = 2$	$c = 4$	$c = 8$
$a = 5$	2.988	2.521	2.521
$a = 10$	1.803	0.818	0.818
$a = 20$	2.037		

	$c = 2$	$c = 4$	$c = 8$
$a = 5$	151	103	103
$a = 10$	114	28	28
$a = 20$	110		

Table 2: Maximum relative difference $\max |q(\mathbf{x}) - q_{ref}(\mathbf{x})| / \max |q_{ref}(\mathbf{x})|$, in the whole ring-shaped channel (in %), of the density ($q = \rho$, left) and the horizontal velocity ($q = u_x$, right) with respect to the reference solution (grid ($c = 4, a = 20$)), for different velocity grids.
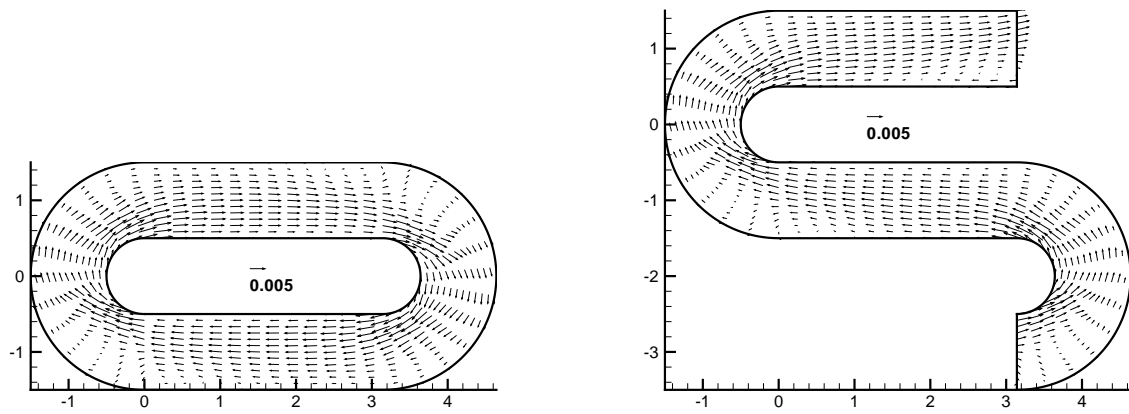
Figure 11: Velocity field in the whole of the ring-shaped channel (left) and in the whole of the S-shaped channel (right). Thick case ($\kappa = 1$) with $Kn = 1$.
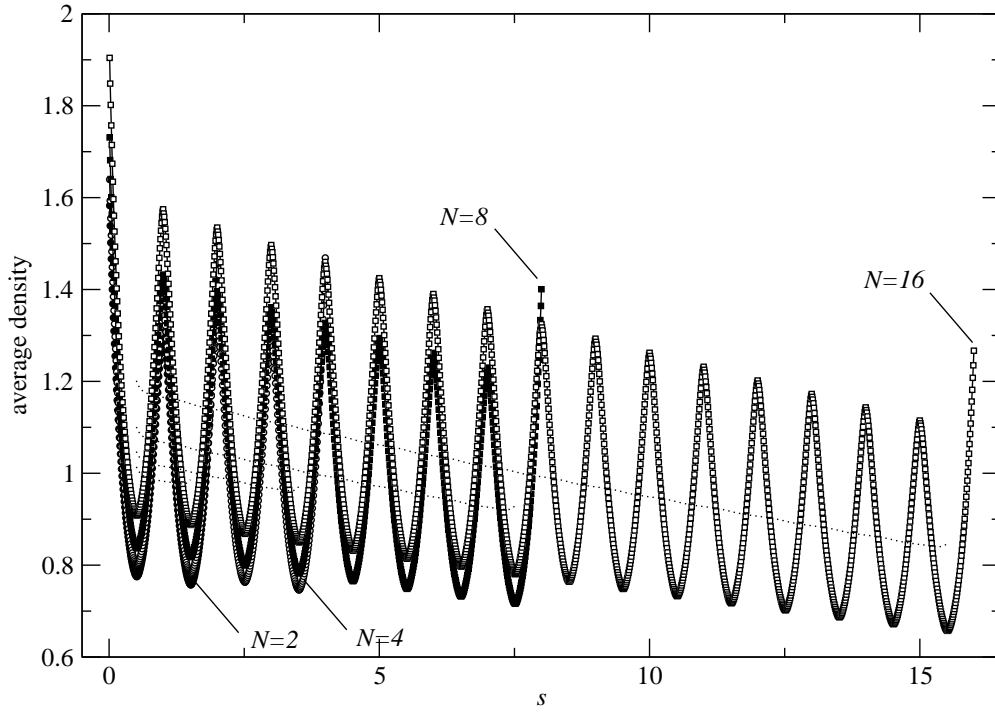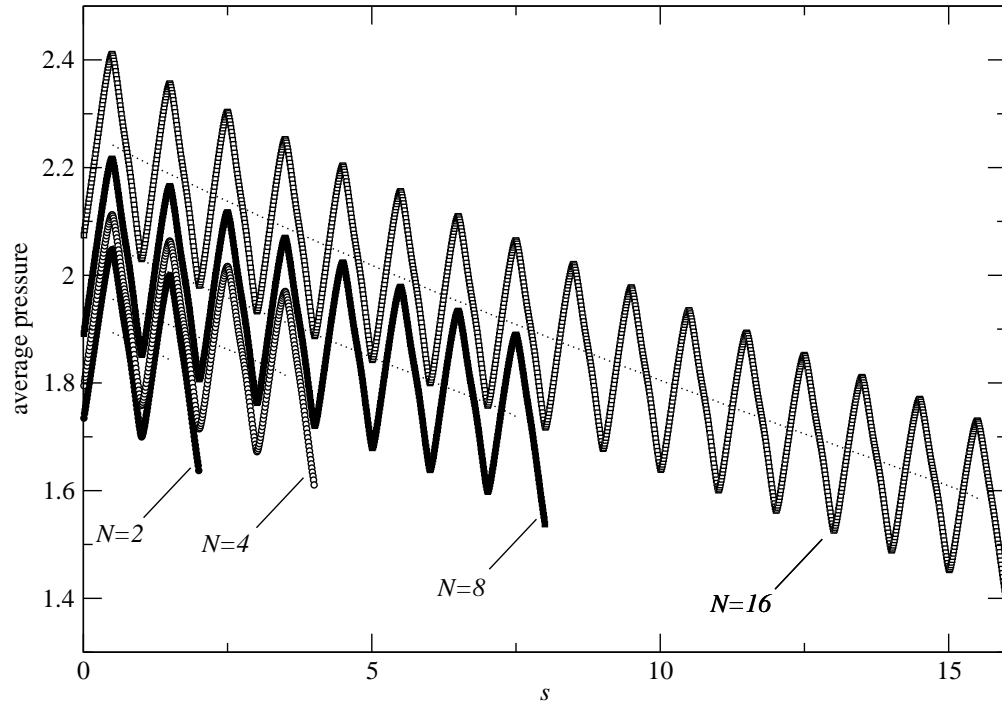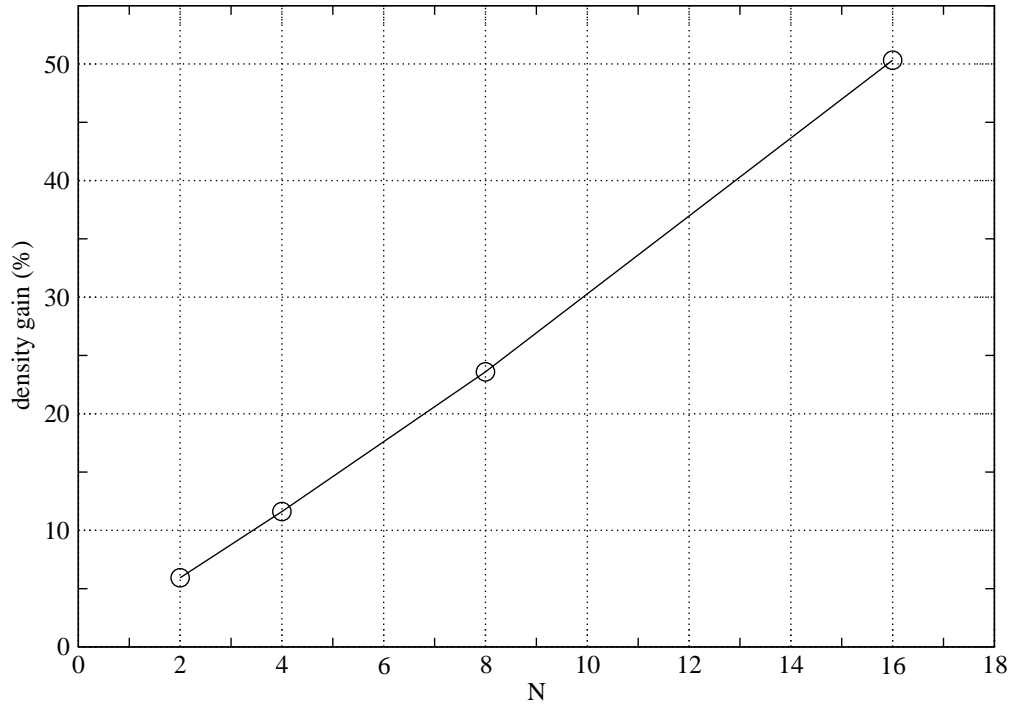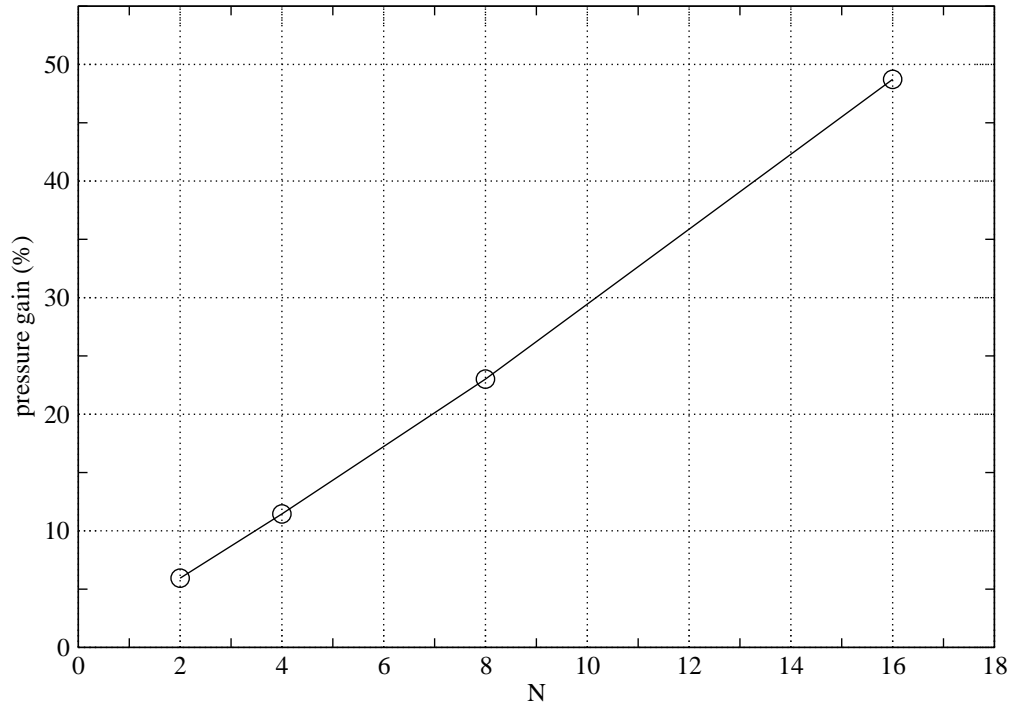
Figure 12: Non-dimensionalized average pressure (top) and density (bottom) profiles as defined in equation (30) for the pumping device (see figure 5) with several numbers N of units. Profiles plotted with black and white circles and squares. The dotted curves are the corresponding profiles obtained by plotting only the average values in each unit. Thick case ($\kappa = 1$) with $Kn = 0.5$.

Figure 13: Pressure (top) and density gain (bottom) as defined in equation (31) for the pumping device (see figure 5) with several numbers N of units. Thick case ($\kappa = 1$) with $Kn = 0.5$.

Temperature $[1.1, 2.8]$

Density $[0.6, 1.9]$
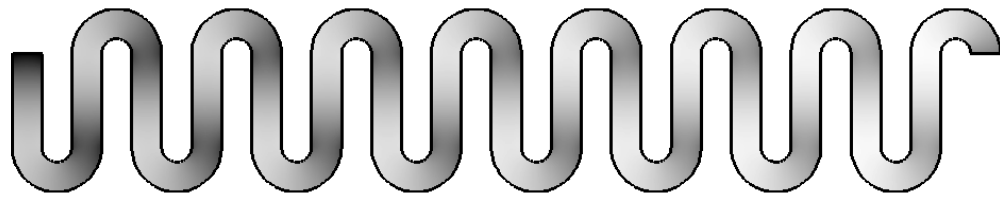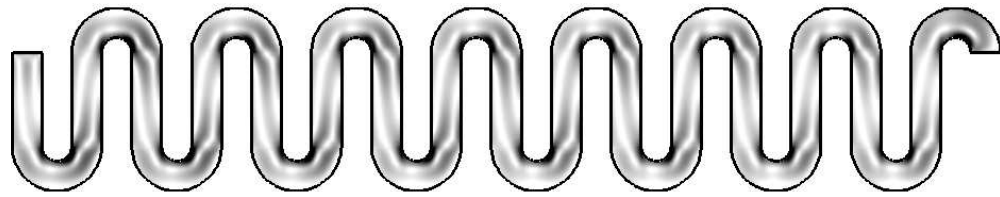
Pressure $[1.4, 2.5]$

Velocity (magnitude) $[0, 0.008]$

Figure 14: Non-dimensional macroscopic fields in the 16 unit pump. For each field, the bounds used for the linear gray-scale is given. Thick case ($\kappa = 1$) with $Kn = 0.5$.
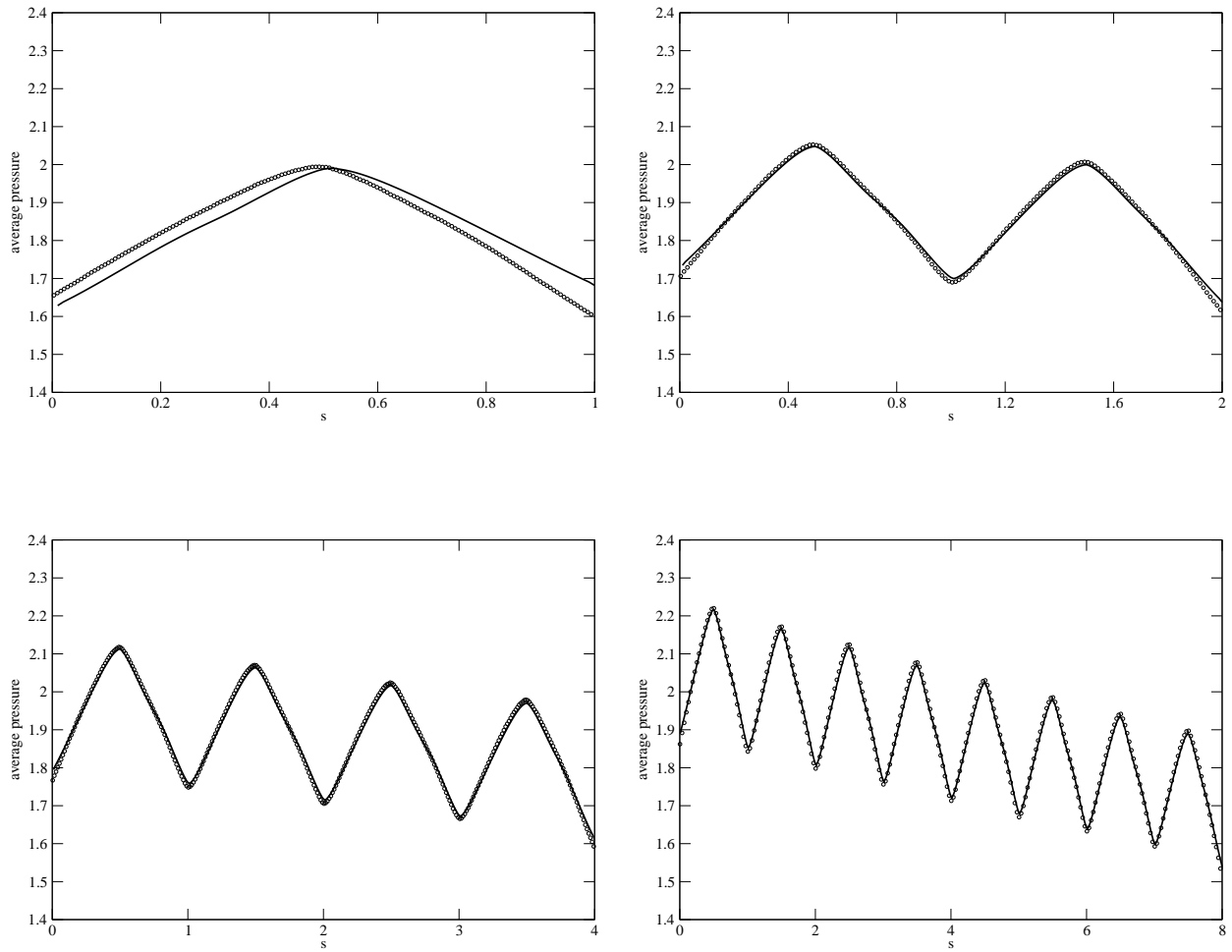
Figure 15: Comparison between BGK (solid line) and Boltzmann-DSMC (circles): non-dimensionalized average pressure profile as defined in equation (30) for the pumping device (see figure 5) for 1 (top, left), 2 (top, right), 4 (bottom, left), and 8 units (bottom, right). Thick case ($\kappa = 1$) with $Kn = 0.5$.
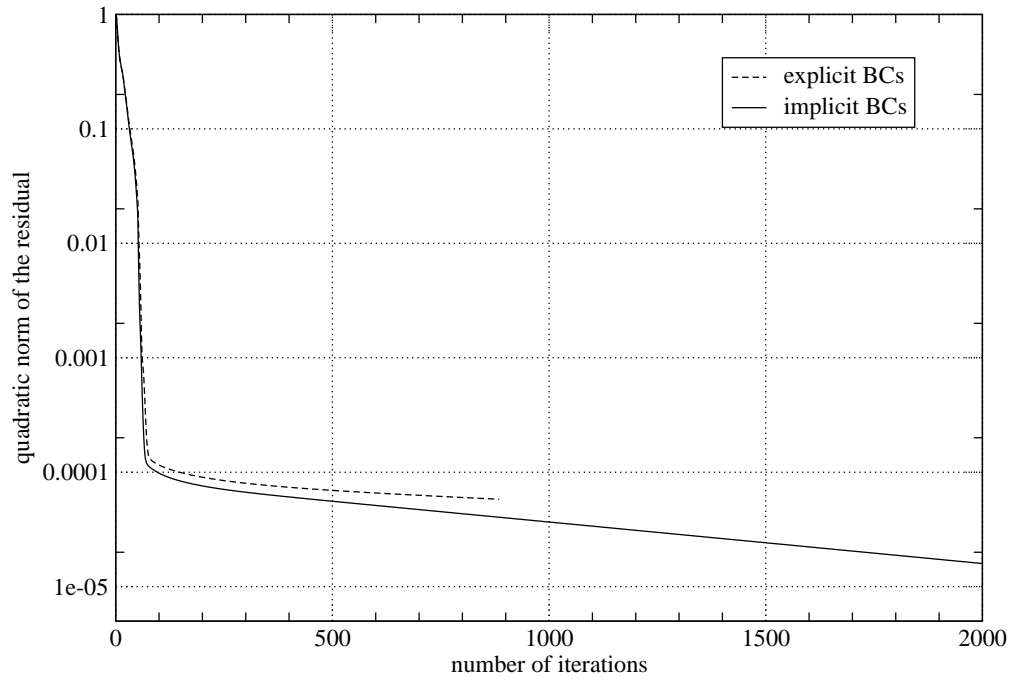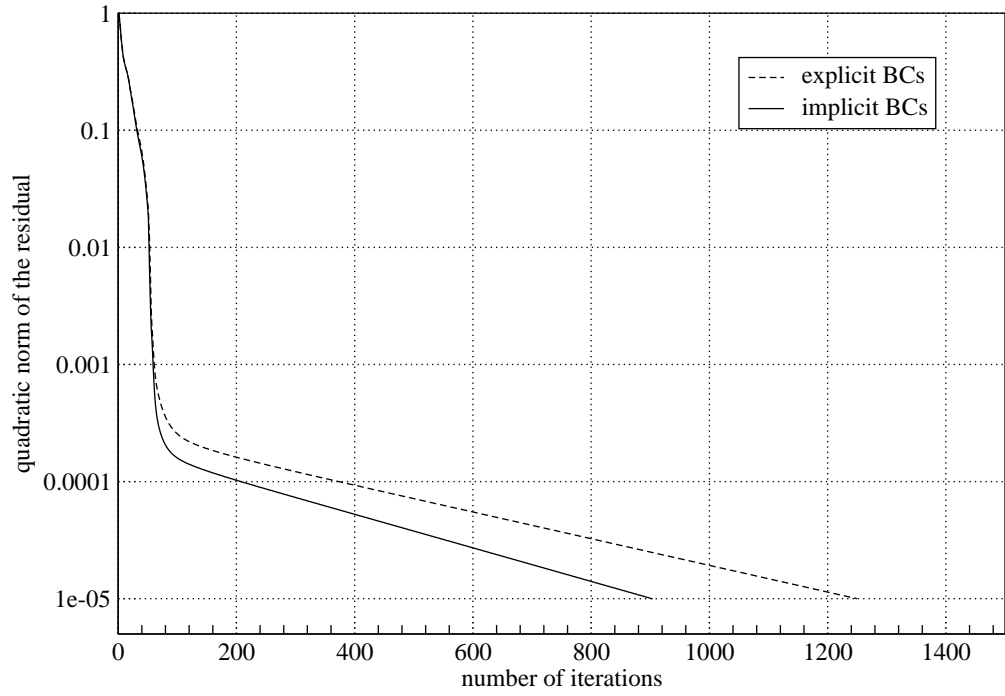
Figure 16: Residual history for 8 units (top) and 16 units (bottom) for the BGK scheme with explicit and implicit boundary conditions. Thick case ($\kappa = 1$) with $Kn = 0.5$.